Title: Single-molecule *in vivo* imaging of bacterial respiratory complexes indicates delocalized oxidative phosphorylation

Authors: Isabel Llorente-Garcia[1,5,+], Tchern Lenn[2,+], Heiko Erhardt[3,+], Oliver L. Harriman[1], Lu-Ning Liu[4,6], Alex Robson[1], Sheng-Wen Chiu[1], Sarah Matthews[1], Nicky J. Willis[4], Christopher D. Bray[4], Sang-Hyuk Lee[2], Jae Yen Shin[2], Carlos Bustamante[2], Jan Liphardt[2], Thorsten Friedrich[3], Conrad W. Mullineaux[4] and Mark C. Leake[1,7,*]

[+]I.L.-G, T.L. and H.E contributed equally to this work.

[*]To whom correspondence should be addressed. E-mail: mark.leake@york.ac.uk

Affiliations: [1]Clarendon Laboratory, University of Oxford, Oxford OX1 3PU, UK, [2]QB3 University of California, Berkeley CA94720, USA, [3]Institut für Biochemie, 79104 Freiburg, Germany, [4]School of Biological and Chemical Sciences, Queen Mary University of London, London E1 4NS, UK Present addresses: [5]Department of Physics and Astronomy, University College London, Gower St., London, WC1E 6BT, UK, [6]Institute of Integrative Biology, University of Liverpool, Liverpool L69 7ZB, UK, [7]Departments of Physics and Biology, University of York, York, YO10 5DD, UK,

Contact: Mark C. Leake, Email: mark.leake@york.ac.uk. Tel: +44 (0)1904 320000. Fax: +44 (0)1904 322214.

Abstract

Chemiosmotic energy coupling through oxidative phosphorylation (OXPHOS) is crucial to life, requiring coordinated enzymes whose membrane organisation and dynamics are poorly understood. We quantitatively explore localization, stoichiometry and dynamics of key OXPHOS complexes, functionally fluorescent protein-tagged, in *Escherichia coli* using low-angle fluorescence and superresolution microscopy, applying single-molecule analysis and novel nanoscale co-localization measurements. Mobile 100-200 nm membrane domains containing tens to hundreds of complexes are indicated. Central to our results is that domains of different functional OXPHOS complexes do not co-localize, but ubiquinone diffusion in the membrane is rapid and long-range, consistent with a mobile carrier shuttling electrons between islands of different complexes. Our results categorically demonstrate that electron transport and proton circuitry in this model bacterium is spatially delocalized over the cell membrane, in stark contrast to mitochondrial bioenergetic supercomplexes. Different organisms use radically different strategies for OXPHOS membrane organization, likely depending on the stability of their environment.

Introduction

Adenosine triphosphate (ATP) is the universal cellular energy currency. The energy released upon hydrolysis of ATP powers many biological processes. Most organisms meet ATP demands by oxidative phosphorylation (OXPHOS), a multi-enzyme process spanning all domains of life using nutrient molecule catabolism. In OXPHOS, electron-transfer reactions between membrane-associated enzymes are coupled via the proton-

motive force (pmf) to ATP synthesis by F_oF_1ATPase [1,2]. Individually, enzymes have been studied extensively for mitochondrial OXPHOS in terms of structure/biochemistry [2], with significant understanding of gene expression/regulation stemming from prokaryotes [3]. However, the system-level architecture and dynamics of OXPHOS membranes is not resolved.

Two principal hypotheses for molecular organization have emerged [4]. In the 'liquid-state' model, individual enzymes are randomly membrane-interspersed, interacting via stochastic mobility. The 'solid-state' model assumes electron flow is mediated through enzyme supercomplexes, functionally and structurally defined regions of the membrane [5-7]. The liquid-state model dominated until supercomplexes, from the bacterium *Paracoccus denitrificans* [8] and mitochondrial inner membrane extracts from plant, yeast and mammalian cells, were isolated by native gel electrophoresis [6,9,10]. In addition, membrane sub-structures consistent with supercomplexes have since been observed by cryo-electron microscopy of inner mitochondrial membranes from plant [11] and mammalian cells [12]. Thus there is strong evidence in support of solid-state models of OXPHOS in eukaryotes and some prokaryotes.

Fluorescence imaging of bacterial OXPHOS in *Bacillus subtilis* [13] and *E. coli* [14,15] have shown mobile membrane patches of enzymes in the cytoplasmic membrane. Also, Halo-Tag imaging of F_oF_1ATPase in inner mitochondrial membrane cristae indicates mobility [16]. The combination of evidence for supercomplexes and diffusive elements led to speculation of membrane 'respirazones': functionally isolated, mobile membrane patches of ~100 nm diameter containing a complement of enzymes necessary for OXPHOS [14,17].

Here, we investigate the native localization and dynamics of several key functional enzymes used in aerobic OXPHOS in *E. coli* by real-time single-molecule fluorescence imaging in live cells. Mobile fluorescent spots were seen in cells expressing fluorescently labelled NDH-1, SDH, Cytochrome bo oxidase and ATP synthase, as expected and similar to the previously observed Cytochrome bd oxidase [14]. Super-resolution localisation microscopy of fixed cells and quantification of fluorescence in live cells confirm that the spots observed contain multiple complexes and in fact represent the positions of clusters of enzymes. Careful categorisation of diffusion reveals that the motion of all of the different complexes observed is similar. However, in contrast to the respirazone hypothesis, we observed that different complexes do not co-localize indicating that both electron transport and the proton circuit are delocalized over the membrane surface. This is very different from the situation in mitochondria where convincing evidence for organization of OXPHOS components into functional supercomplexes suggests localization of electron transport. We discuss functional and evolutionary implications of these different strategies below.

Results

OXPHOS enzymes are in cell membrane patches extending several tens of nm

E. coli strains were engineered by 'scarlessly' replacing the native allele of interest on the genome with genes for fluorescently labelled proteins – GFP or mCherry fused with subunits of one of five OXPHOS enzymes. The resulting strains contained no antibiotic resistance cassettes on their genomes to interrupt transcription of the operons to which our genes of interest belong. The subunits labelled were NuoF of NADH dehydrogenase

(NDH-1), CydB of cytochrome bd-I complex, CyoA of cytochrome bo_3 complex, AtpB of F_oF_1ATPase, and SdhC of succinate:fumarate oxidoreductase (SDH). The fluorescent proteins had only marginal effects on cell growth and OXPHOS in comparison with wildtype strains (Supplementary Table S1), indicating little perturbation of function. Further tests that thoroughly characterise the functionality and fidelity of labelling in our strains can be found in Erhardt et al 2014 [18]. We immobilized cells from exponentially growing cultures on poly-L-lysine coated glass coverslips of a ~5 μl microscope flow-cell and visualized the dynamic fluorescent protein distribution in single cells using real-time imaging by near-total internal reflection fluorescence (TIRF) excitation [19] on a bespoke single-molecule microscope [20] permitting simultaneous imaging of GFP/mCherry on separate halves of the camera with insignificant bleed-through or cross-talk between fluorescent proteins detected in their respective green and red channels (Fig. 1a).

Strains expressing single OXPHOS fusions with either GFP or mCherry had distinct spots of fluorescence in the cytoplasmic membrane ~300-500 nm full width at half maximum (FWHM) diameter, 50-200 nm larger than the measured point spread function (PSF) width of our microscope [20]. As previously suggested, the difference between the FWHM of the detected spots and the measured point spread function of the microscope estimates the real dimensions of the structure producing the spots [14]. After an initial period of a few seconds, in which the bulk of the fluorophores photobleached, ~1-5 spots were detected per cell from individual image frames, with no obvious cellular positional dependence (Fig. 1b) as observed previously using TIRF on a strain expressing CydB-GFP [14].

Higher-resolution data were obtained using photoactivated localization microscopy (PALM) [21] with photoswitchable fluorescent protein mMaple [22] fused to CydB and NuoF in fixed cells. PALM images indicate clusters of localizations in the cell membrane over a similar length scale (50-200 nm) as predicted above from spots in near-TIRF imaging (Fig. 1c and Supplementary Figure 1).

We then investigated and more thoroughly analysed three dual-labelled strains expressing NuoF-GFP:SdhC-mCherry, AtpB-GFP:CydB-mCherry and NuoF-GFP:CydB-mCherry to monitor simultaneous localization of pairs of tagged OXPHOS proteins. Near-TIRF images were recorded over ~10 s at a 25 Hz frame rate. Dual-color images indicated similar spots of fluorescence as seen for single-labelled strains, with movie data showing some spots are mobile across the cell membrane surface (Supplementary Movies S1, S2), as observed previously [14], while a proportion are relatively immobile, indicated by comparatively unblurred fluorescence foci on frame averaged images generated from data sequences over several seconds (Fig. 1d upper panel).

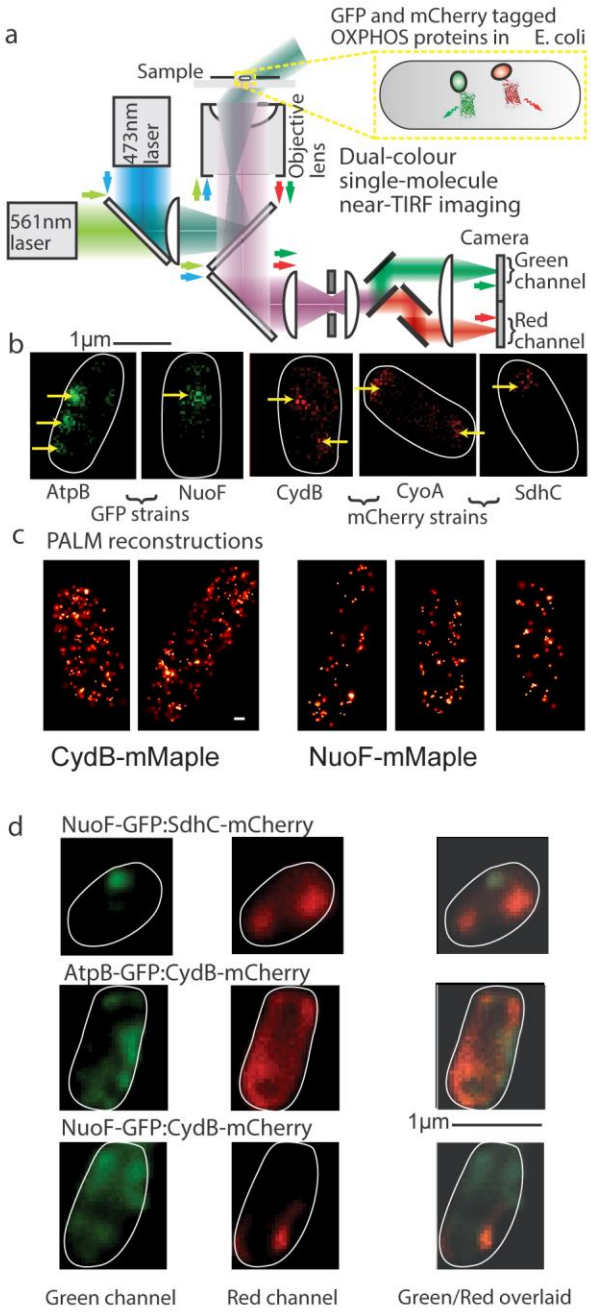

Fig. 1. Near-TIRF microscopy of OXPHOS proteins in *E. coli*. **(a)** Schematic of dual-color near-TIRF imaging microscope. **(b)** Single near-TIRF image frames (40ms exposure) of single-labelled GFP and mCherry OXPHOS cell strains, distinct fluorescent spots indicated (yellow arrows) and cell body border based on brightfield images (white). **(c)** Typical PALM reconstructions for mMaple-labelled strains with putative membrane patches. White bar indicates 200 nm. See materials and methods for image rendering information. **(d)** Frame average images of dual-labelled cell strains, red (left panel) and green (centre panel) and overlaid channel (right panel) shown.

There is a broad range in stoichiometry between different OXPHOS enzymes and different patches

Diffusing spots of fluorescence were tracked in each separate color channel for at least five consecutive image frames, with some tracks lasting several seconds. We then calculated the stoichiometry of each detected spot *in vivo* by simple ratio of the initial intensity of each track to the brightness of single fluorescent protein molecule as described in *Materials and Methods*. The distribution of stoichiometry for each strain was generated using unbiased kernel density estimation [23], a technique (alternative to the use of histograms) that convolves the raw data using Gaussian functions to represent each measurement and its error, and which results in an objective final distribution of measurements that is not biased by subjective and arbitrary histogram bin widths and edge positions. The distributions indicate a broad range in number of molecules per spot (Fig. 2 and Table 1). For dual-labelled strains (Fig. 2a-c), the distributions indicate FWHM ranges of 10-20 and 20-40 molecules per spot for NuoF and SdhC respectively, 40-60 molecules per spot for AtpB, and, similar to an earlier study [14], 70-180 molecules per spot of CydB (Supplementary Figure 2 indicates example *in vivo* photobleach traces compared to purified single surface-immobilized fluorescent protein molecules obtained under the same imaging conditions). Spots from the same cells ranged in stoichiometry across the full range of these distributions. In addition to the dual-labelled strains, which gave information for four of the OXPHOS complexes, we investigated the stoichiometry of spots in a single-labelled strain expressing a genomic mCherry fusion of the terminal oxidase CyoA, containing 25-45 molecules per spot (Fig. 2d). Calculations based on cell doubling times and fluorescence maturation data

indicate less than 1% of the proportion of fluorescent protein is in an immature 'dark' state [20]. We note that while it may be tempting to calculate the number of patches per cell taking into account our results and combining them with possibly available measurements of total numbers of OXPHOS proteins per cell from high-throughput studies (see for instance Taniguchi *et al.* [24]), significant differences in the details of the techniques used for each type of measurement make these studies not immediately comparable. In particular, there are significant genetic differences (our study uses specific linkers and mutations which are 'scar-less' in nature, compared to generic linkers and issues with antibiotic-resistance cassette remains in the above mentioned high-throughput study), as well as differences in growth and imaging conditions that preclude direct comparison.

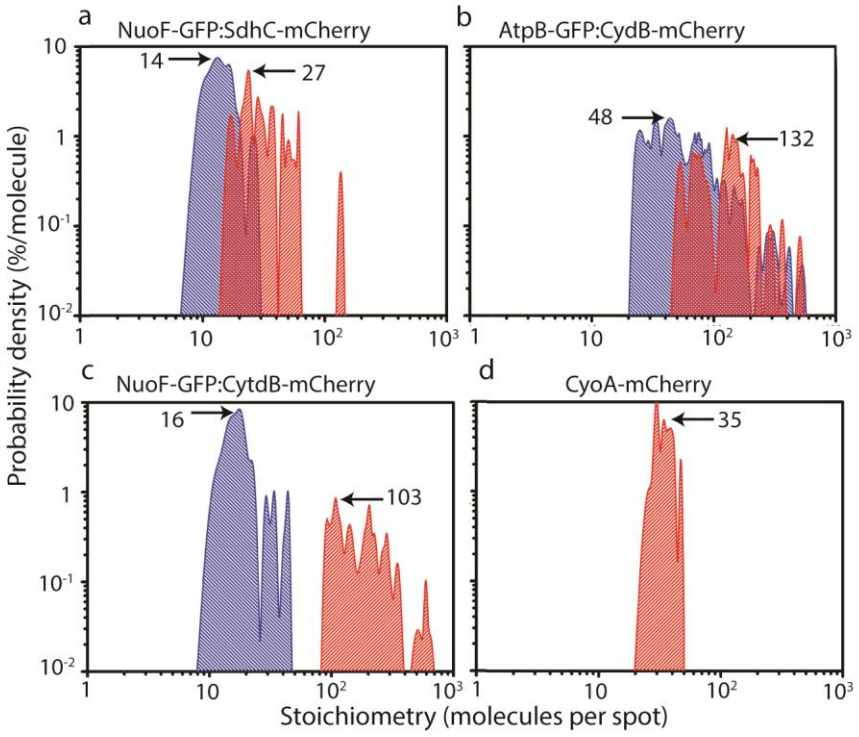

Fig. 2. Stoichiometry of OXPHOS complexes. Unbiased kernel density estimations for numbers of OXPHOS protein molecules per fluorescent spot, for **(a)-(c)** dual-labelled cell strains and **(d)** the CyoA single-labelled strain. GFP (blue) and mCherry (red) components shown, with peak value (arrow). *n*=18-134 tracks analysed.

OXPHOS protein (Source cell strain)	**Peak stoichiometry ±HWHM (molecules per spot)**
NuoF (NuoF-GFP:SdhC-mCherry)	16±4
NuoF (NuoF-GFP:CydB-mCherry)	14±6
SdhC (NuoF-GFP:SdhC-mCherry)	27±10
AtpB (AtpB-GFP:CydB-mCherry)	48±13
CydB (NuoF-GFP:CydB-mCherry)	103±33
CydB (AtpB-GFP:CydB-mCherry)	132±46
CyoA (CyoA-mCherry)	35±8

Table 1. OXPHOS protein stoichiometry values in cytoplasmic membrane patches, using peak value from Gamma fit to the kernel density estimation for stoichiometry distribution, with corresponding half width at half maximum (HWHM) fit values indicated.

OXPHOS patches exhibit confined and unconfined diffusion

The diffusion of OXPHOS complexes in dual-label strains was characterized using BARD analysis [25] which applies Bayesian inference to determine the most likely type of diffusion (from either confined, anomalous, normal/Brownian, or directed diffusion) from experimental trajectory data from tracked spots. The proportions of tracks assigned to each diffusion type for all tagged complexes in all strains analysed are shown in Supplementary Table S3. Supplementary Table S4 shows the frequencies of tracks which are confined or unconfined (anomalous, Brownian or directed) for the dual-label strains. On average 47% ± 10% (± s.d.) of tracks have confined mobility and 53% ± 10% (± s.d.) have unconfined mobility, consistent across the dual-label strains to within the error of the BARD analysis. A two-way chi-squared test of the diffusion categorizations for NuoF, CydB, SdhC and AtpB, yielded a non-significant result: $\chi^2 = 4.306$ (Pearson's chi-squared test statistic); N = 342 (total number of tracks analysed); d.f. = 3 (number of degrees of freedom); $P = 0.23$ (*P*-value, probability). It is therefore unlikely that these four OXPHOS proteins differ from each other in terms of their 'preference' for diffusion type.Roughly half of the unconfined spots were anomalous/sub-diffusive, while the remainder were Brownian at mean rate 0.007 ± 0.005 $\mu m^2 s^{-1}$ (±s.d.) across all strains (Supplementary Figure 3a). For confined spots (Supplementary Figure 3b,c) we found confinement domains with mean effective radius 0.05 ± 0.02 μm (±s.d.), which is greater than our localization precision. We observed no dependence on either diffusion coefficient or confinement radius with number of fluorescent proteins in each spot (Supplementary Figure 4).

Our trajectory measurements are in principle a projection onto the camera imaging plane of the three-dimensional diffusion movement of the complexes within a curved bacterial membrane of capped-cylindrical shape. However, both our measured confinement radius of 0.05 ± 0.02 μm (±s.d.) and measured total displacements of labelled OXPHOS proteins diffusing in the membrane (particularly the transverse displacements, perpendicular to long axis of bacterial body), are an order of magnitude smaller than the width of a cell body (~1 μm), such that effects of curvature [26,27], of the cytoplasmic membrane are likely to be small within the area explored by the diffusing protein complexes, consistent with BARD mobility analysis indicating no significant difference in the one-dimensional diffusion coefficients estimated from trajectory data parallel to the cell long-axis compared to those perpendicular to the long-axis. In particular, given our experimental imaging frame rate, the typical width of *E. coli* bacteria and the expected range of diffusion coefficient values, according to reference [27], the underestimation bias resulting from membrane curvature for our diffusion coefficients is negligible.

Although the mean value of diffusion coefficient of ~0.007 $\mu m^2 s^{-1}$ across all strains was smaller than that measured from an earlier study in reference [14] obtained using single particle tracking of CydB-GFP, the range of diffusion coefficients estimated for the CydB-mCherry strain in our study here (Supplementary Figure 4a) was within experimental error to that measured for the CydB-GFP previously when comparing equivalent levels of molecular stoichiometry.

Different OXPHOS enzymes assemble in different patches

The aforementioned respirazone hypotheses predicts co-localization of OXPHOS complexes in ~100 nm patches – patches smaller than the resolution limit of the microscope – and we have already observed that the patches are dynamic. We therefore determined how frequently signals in the red and green channels were co-localized in order to see if co-localization occurred more frequently than by chance, given the observed density of proteins in the membrane.

To quantify co-localization, we implemented several complementary approaches. We first investigated co-localization at the length scale of the whole cell (a), both looking at frame averages (time scale of seconds) (a.1) and at single frames (frame-by-frame, time scale of 40 ms) (a.2), for all image sequences in each dual-label-strain data set. The second approach (b) consisted of calculating the overlap of individual fluorescent spots tracked on both channels simultaneously.

(*a*) *Whole cell method.*

We generated co-localization maps for each cell, using the difference in normalized fluorescence intensities on a pixel-by-pixel basis between corresponding pixels in the green and red channels inside each cell boundary. The analysis output is a pixel map of coefficients, with values of -1 and +1 corresponding theoretically to features present only in green or red channels respectively whereas values clustered around zero indicate features common to both channels.

(a.1) Looking at frame averages:

A color map and histogram of co-localization values was produced for each frame-averaged fluorescence image sequence in a data set in order to generate qualitative

estimates from our dual-labelled data; spots tracked on both channels presented typically a relatively low mobility over our time scale of observation, still appearing very clearly on images after frame averaging for at least ~10 s.

Fluorescence frame averages were calculated and separated into their red and green channels and any spatial translation between images acquired on the red and green channels was determined as described in the Materials and Methods section. For both channels, a region of interest around the cell body was selected and pixel-thresholding employed to define 'cell masks' in both channels to isolate cell fluorescence from the image background. Both channels were then re-scaled to normalize pixel intensities between 0 and 1.

The difference between re-scaled translated red channel and re-scaled green channel intensity values was then calculated for each pixel. These final co-localization values were plotted on a color map (see example on Fig. 3a), with values close to +1 representing bright features found on the red channel but not on the green channel, values close to -1 representing bright features on the green channel but not on the red channel, and values around 0 corresponding to features common to both channels in terms of normalized brightness (including any putative co-localized bright spots on the frame averages).

With this qualitative method, it is clear that over a time scale of seconds the different OXPHOS complexes do not on average occupy similar locations in the cell membrane, and that the low-mobility patches do not contain different OXPHOS complexes.

(a.2) Frame-by-frame approach:

Co-localization was also analysed on a frame-by-frame basis by following the same process as outlined above, but applied to single frames (see Fig. 3b) instead of frame averages, which rendered co-localization data over an effective time scale of seconds, to probe smaller time scales of tens of ms while still obtaining a measure of co-localization averaged over single whole cells. Co-localization values (see Fig. 3c) were calculated for each of the first 25 frames in a given fluorescence image sequence, and then accumulated together to produce histograms such as those in Fig. 3d. Such histograms or distributions of co-localization coefficients could be fitted to a sum of three Gaussian curves with their centres constrained to be in the ranges -0.4 to -0.1, 0, and 0.1 to 0.4 and their widths in the ranges 0.15-0.25, 0-0.5, and 0.15-0.25, respectively. These constraints came from applying the same analysis method to single-label-strain data acquired under the same imaging conditions as the dual-label data; the analysis of images with fluorescence present on one of the channels only, with only noise on the other channel, yielded distributions of co-localization values whose magnitude was centred typically around 0.2-0.3, with standard deviations of ~0.2.

The fraction of brightness features which appeared to be co-localized on both channels was estimated for the dual-label data as the fraction represented by the area under the Gaussian curve centred around zero, out of the total area under the sum of the three Gaussian curves. Note that when applied to single-label data, this method yielded, as expected, fractions of brightness corresponding to the actual fluorescence channel in excess of 90% (96 ± 4 % (±s.d.)) and very small fractions (3 ± 4 % (±s.d.)) under the central Gaussian. The contribution to the co-localized fraction due to random image noise

is therefore very small. The co-localized fractions estimated provide an upper threshold to the degree of intrinsic co-localization between different observed OXPHOS protein complexes, given unavoidable small contributions due solely to co-localized background features.

For all dual-label image sequences analysed, there was excellent agreement of the qualitative color maps of co-localization values obtained from frame averages, with the corresponding fractions of co-localized brightness and of brightness coming from either the red or green channels, obtained from sets of single frames.

Therefore, for each dual-labelled strain, the area under the central Gaussian curve as a fraction of the total, indicated the proportion of pixels with common red/green features (Table 2), indicating a mean value of 22 ± 7 % (±s.d.) across the three dual-label data sets. The individual fractions obtained for each data set can be seen in Fig. 3e.

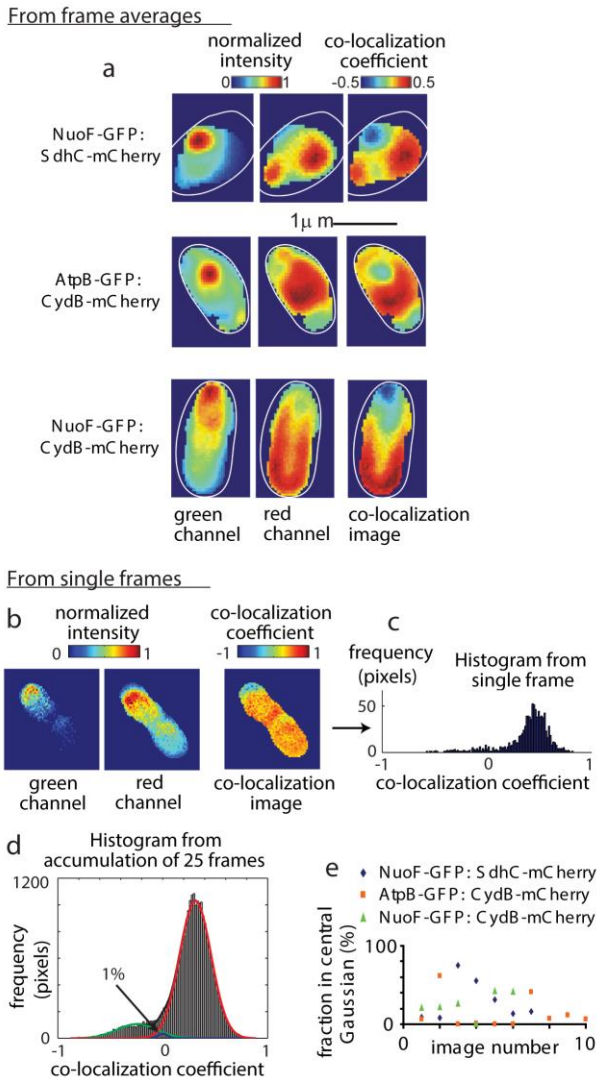

Fig. 3. OXPHOS protein co-localization analysis, whole-cell method. **(a)** Typical frame-average dual-labelled cell strain near-TIRF images with cell borders shown (white), normalized intensity (false-color) for GFP (left panel) and mCherry content (centre panel), and frame average co-localization pixel map (right panel); **(b)** Typical single-frame dual-label data with GFP (left) and mCherry (centre) normalized intensity channels, and with single-frame co-localization map (right); **(c)** Example distribution of co-localization values from the single-frame map in (b) (right); **(d)** Example distribution of co-localization coefficients formed by accumulating values from 25 single frames in a given image sequence (same one as for b and c), showing fit to a sum of three Gaussians (black) as well as the individual Gaussians for GFP (left, green) and mCherry (right, red) channels, and central Gaussian in blue. The central blue Gaussian indicates features common to both color channels and the percentage area under it of the total (indicated %) gives a measure of the co-localized fraction; **(e)** Co-localization fractions (%) (fractional area under central Gaussian, data from 25 frames) for all image sequences analysed in all three dual-labelled strains.

(b) Tracked spot method.

The most robust quantitative metric for co-localization utilized single particle tracking of fluorescent spots in each color channel. We identified green and red channel tracks at least five consecutive image frames in duration which were coincident in time, and constructed an analytical overlap integral function modified from an earlier method [28]. We considered all frames for which bright spots had been detected and tracked on both red and green channels simultaneously. For these spots detected at coincident times on both channels, we used the Gaussian-fit parameters (amplitude, centre and width) obtained from the previous tracking analysis of the image sequences, taking into account the appropriate spatial translation between the red and green channels for each image sequence. This shift was pre-calculated from the corresponding brightfield images which bled through into each channel, in the same way as described for the whole cell methods, by finding the position of best overlap of the red and green channels, i.e. the maximum of their cross-correlation function (see Materials and Methods). The Gaussian intensity profiles of the bright spots were normalized by dividing by their fitted Gaussian amplitudes and, for each time-overlapping track pair, the overlap of the Gaussian spots (overlap integral, v, see Materials and Methods) was calculated on a frame-by-frame basis. The overlap integral can take values between 0 (no overlap) and 1 (complete overlap). We made use of a modified Rayleigh-type resolution criterion and considered that two spots were co-localized when their overlap was large enough or, in other words, when they could not be 'resolved' due to their separation on the image being below ~2.5 times their Gaussian width. The actual Rayleigh resolution criterion states that two spots

can only be resolved when their separation is large enough such that at least the maximum of one of the Airy-diffraction patterns is at the same position as the first minimum of the diffraction pattern from the other spot. Though we used Gaussian function approximations to Airy functions to fit the intensity pattern of each detected spot we can still define a similar criterion, considering that at a distance from the centre of ~2.5 times the Gaussian width, which encapsulates 99% of the total area under the Gaussian curve.

Therefore, we considered two spots as co-localized when their separation was below 2.5 times their Gaussian width. For two equal-width Gaussians separated by 2.5 times their width, the overlap integral takes a value of ~0.2 and hence, our criterion considered two spots as co-localized if their overlap integral was above 0.2. This threshold-overlap value would change for spots of different widths, however, the widths of the spots detected on both channels were very similar, and the distributions of width ratios (σ_1/σ_2) obtained from all spot pairs for this analysis were centred around 1 and had standard deviations of 0.1-0.2.

The overlap integral value for each red-green track pair (see Fig. 4a) was calculated as a function of relative separation between red-green spot intensity centroids, and of spot widths. For each time point this resulted in an overlap number in the range 0-1 (see Fig. 4b), with 0 indicating no overlap and 1 that both spots are precisely co-localized. The distribution of overlap integral values across all three dual-labelled strains is shown in Fig. 4c, where the theoretical co-localization threshold of 0.2 such that two spots are no longer resolved independently has been indicated. Our results indicate a mean of 17 ± 4% (± s.d.) time points have an overlap integral in excess of 0.2 (Table 2).

We used a Poisson nearest-neighbour model to characterize the distribution of spots in the cell membrane and calculate the probability of chance co-localization (see Materials and Methods). The theoretical likelihood for observing chance co-localization within the optical resolution limit of our microscope of different OXPHOS complexes is 24%, based on the observed surface density of spots in the cell membrane, taking into account the width, length and shape of the bacterial cells, and the measured point spread function width of our microscope. The proportions of pixels observed indicating putative co-localization from all of our analysis methods at both the whole cell and single tracked spot levels are on average below or consistent with this 24% chance co-localization threshold, indicating that the observed co-localization is due to single, unassociated spots from different color channels overlapping within the optical resolution limit, rather than to different OXPHOS enzymes associated as a supercomplex.

Strain name	**Mean co-localized fraction of pixels using whole cells ± s.e.m. (%)**	**Proportion of spot pairs with overlap integral >0.2 of all spot pairs coincident in time (%)**
NuoF-GFP:SdhC-mCherry	30 ± 10	17
AtpB-GFP:CydB-mCherry	14 ± 7	13
NuoF-GFP:CydB-mCherry	25 ± 6	21

Table 2. Co-localization fractions of pixels for dual-labelled OXPHOS cell strains from whole cell images based on 3-Gaussian fit method using n = 7-10 cells (column 2) (see also Fig. 4e), compared against proportion of spot pairs that are within the optical resolution limit of each other (column 3), n=24-468 spot pairs analysed.

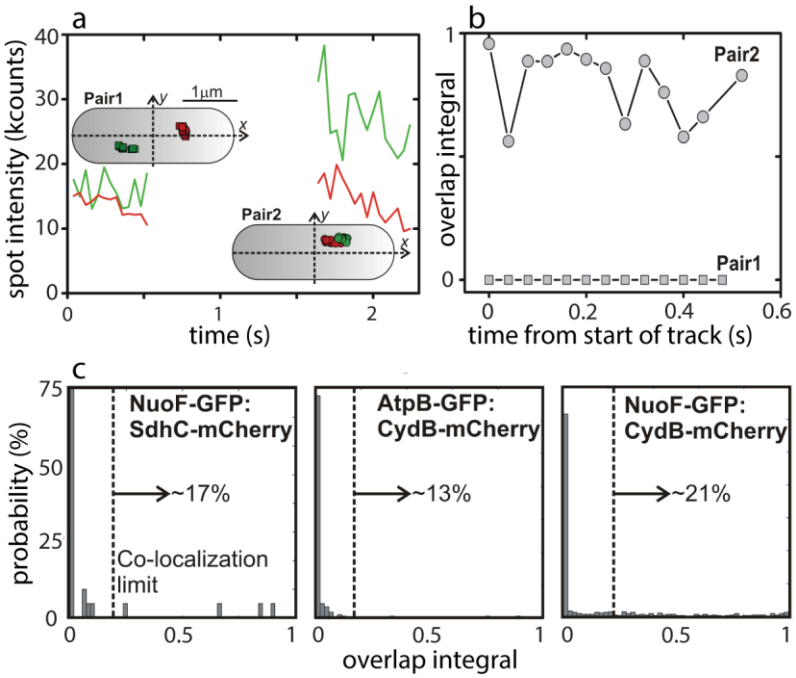

Fig. 4. OXPHOS protein co-localization analysis, tracked spot method. **(a)** Intensity versus time traces for two typical tracked spot pairs coincident in time for cell strain AtpB-GFP:CydB-mCherry, GFP (green) and mCherry (red) spots overlaid on schematic cell coordinate system (grey); **(b)** Pair-1 (squares) and pair-2 (circles) from (a) indicating low and high levels of spot overlap respectively. The calculated overlap integral is shown as a function of time from the start of the track; **(c)** Distributions of overlap integrals for all spot pairs coincident in time, for all dual-labelled strains, with percentage of spots separated by less than the co-localization limit indicated (arrow). The number of spot pairs analysed was *n*=24-468.

Ubiquinone mobility is correlated to respiratory activity

In order to compare the distribution and dynamics of the mobile electron carrier ubiquinone with those of the OXPHOS enzymes, *E. coli* cells were incubated with OXPHOS active, fluorescently-labelled ubiquinone, NBDHA-Q [29]. Confocal imaging indicated halos consistent with cell membrane localization with no indication of distinct spots (Fig. 5a), which contrasts the patchy distribution of OXPHOS complexes seen above. To clarify if NBDHA-Q was located in outer or inner cell membranes, we elongated cells using cephalexin [30] on agar plates with 15% sucrose for osmotic shock treatment [31] resulting in inner membrane invagination, subsequent imaging indicating cytoplasmic membrane localization (Fig. 5b). Estimates for ubiquinone diffusion coefficient were obtained using fluorescence recovery after photobleaching (FRAP) (Fig. 5c).

FRAP data were modelled by relating changes in bleach profile with respect to time to effective diffusion coefficient [32], indicating temperature-dependent diffusion from $1.0 \pm 0.3\ \mu m^2\ s^{-1}$ at 15°C up to $1.8 \pm 0.3\ \mu m^2\ s^{-1}$ (± s.d.) at 37 °C (Fig. 5d, Table 3), roughly correlated to respiratory activity as assessed by cellular oxygen uptake which could be modelled using a Boltzmann factor [33] whose activation barrier was ~18 kcal/mol, comparable to ATP synthesis requirements (Supplementary Figure 5).

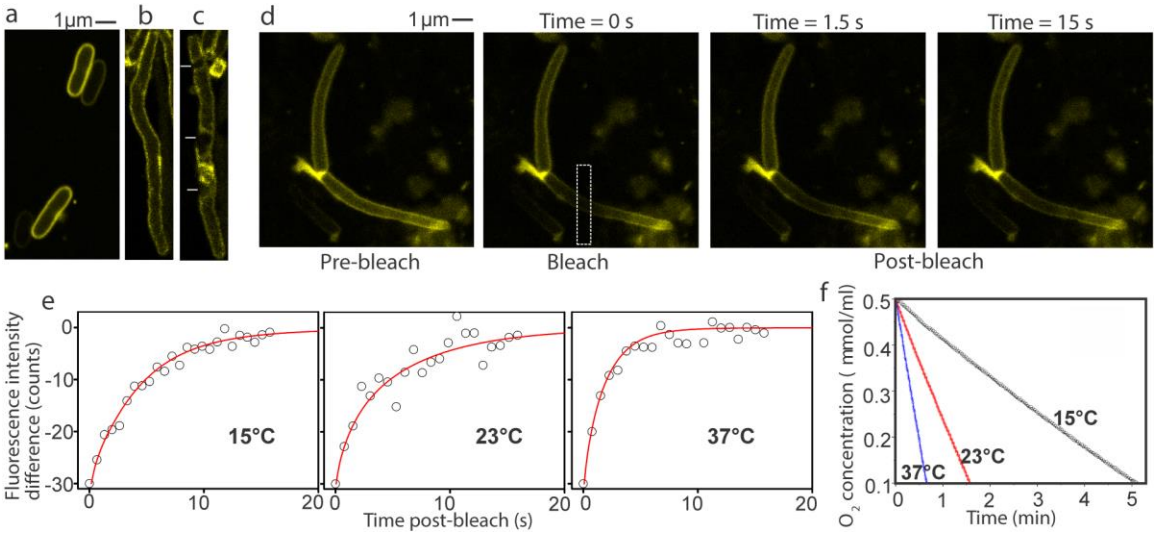

Fig. 5. Ubiquinone mobility in live bacteria. **(a)** Confocal images of *E. coli* cells incubated with NBDHA-Q, with **(b)** cephalexin-elongated cells pre and **(c)** post osmotic shock, cytoplasmic membrane invagination indicated (arrows). **(d)** FRAP of cephalexin-elongated cells, initial laser bleach region indicated (rectangle). **(e)** Example recovery of fluorescence intensity with time (circles) with fit to generate optimized diffusion coefficient estimate (red) for three different cells, mean and s.d. diffusion coefficient at each temperature estimated using *n*=15 cells for each temperature. **(f)** Oxygen uptake at three different sample temperatures using *n*=3 separate cultures.

Temperature (°C)	**Diffusion coefficient ± SD ($\mu m^2 s^{-1}$)**	**Oxygen uptake rate ± SD ($\mu mol\ ml^{-1}\ h^{-1}$)**
15	0.96 ± 0.26	0.590 ± 0.007
23	1.26 ± 0.23	2.260 ± 0.003
37	1.79 ± 0.33	5.362 ± 0.048

Table 3. Variation of effective diffusion coefficient for fluorescently-labelled ubiquinone, as estimated using FRAP, and oxygen uptake rates with respect to temperature.

Discussion

All the OXPHOS complexes that we examined in *E. coli* appear to be packaged in clusters of like complexes. The pairs of complexes that we examined (NDH-1 with cytochrome bd-1; cytochrome bd-1 with F_oF_1ATPase; NDH-1 with SDH) show no significant co-localization, indicating that different complexes are packaged into different clusters, suggesting a form of architecturally segregated zones in the cell membrane, which we call 'segrezones'. There have been several previous studies *in vitro* suggesting close associations between different mitochondrial OXPHOS enzymes in addition to cryo-EM data from functional mitochondria [6,11,12]. There are also *in vitro* studies in bacteria aside from *E. coli* [8,34]. Recent studies in *E. coli* suggest associations of NDH-1/NDH-2 and cytochrome bd-I/cytochrome bo_3/FDH , and cytochrome bd-II/SDH [35]. We did not test these pairs of complexes in our study, as we were interested in complex pairs that are predicted to be functionally complete electron and proton pathways *in vivo*. Our results suggest that 'respirazones' [17] previously hypothesized, as distinct phospholipid patches containing multiple respiratory enzymes, are unlikely to be prevalent in native *E. coli* membranes.

The physical explanation for clustering is not clearly established, but might be facilitated by protein-protein interactions and lateral segregation of membrane lipids. Previous fluorescence imaging monitoring phase transitions in artificial giant unilamellar lipid vesicles indicates the presence of distinct patches composed of a lower viscosity phase surrounded by a phospholipid sea of higher viscosity [36]. Characterizing such liquid domains using a two-dimensional Ising model predicated several metastable

patches of phospholipids, whose effective width covers the range of length scales we observe here [37].

Alternatively, clustering could be effected by protein-protein interactions through entropically-driven aggregation in which collections of neighbouring proteins are probabilistically driven closer by a 'depletion' force [38]. In support of this, Monte Carlo simulations based on another bioenergetic membrane, developing chromatophore membranes in purple photosynthetic bacteria, illustrate the potential for entropically-driven sorting of protein complexes of like size and shape into separate domains [39]. The sorting of complexes into such domains may serve as an efficient way to pack protein complexes into a crowded membrane, however this may not solely explain our lack of observed non-random co-localization.

Our observations here did not indicate a significant variation of diffusion coefficient with stoichiometry, in addition calculations based on a comparison of the physical size of OXPHOS enzymes compared to the patches indicate less than 30% of a patch is occupied by fluorescently-labelled OXPHOS protein [14], suggesting they consist of loose assemblages and that the observed movement of fluorescent spots is due to the motion of a whole patch as opposed to tightly-bound multimers/supercomplexes.

A significant proportion of patches were immobile beyond a length scale of ~100 nm, in contrast to earlier imaging observations in artificial lipid vesicles in which similar sized patches experienced exclusively Brownian diffusion [36]. This may indicate the source of confinement derives not from intrinsic lipid bilayer architecture but from an extrinsic origin, such as the cytoskeleton or the effects of crowding from membrane-integrated proteins [40].

One of the pairs of OXPHOS complexes we examined constitutes the two enzymes involved in a major *E. coli* electron transport pathway: NADH to oxygen *via* NADH dehydrogenase and cytochrome bd-I. These enzymes are thought to be co-regulated at the transcriptional level and be the major route of electron flux from NADH to oxygen under microaerobic conditions [3,41]. The absence of any clear co-localization between NDH-1 and cytochrome bd-I (Fig. 1d lower panel) indicates there is no supercomplex involved in this pathway. Electron transport between the two complexes is mediated by ubiquinone [42], and our FRAP data indicate ubiquinone diffusion is ~2 orders of magnitude faster than diffusion of the membrane patches (Fig. 5). This suggests electron exchange between NADH dehydrogenase and cytochrome bd-I is mediated by long-range diffusion of a ubiquinone pool that is delocalized in the membrane. Furthermore, modelling the change in diffusion coefficient with temperature using a heuristic power-law (Supplementary Figure 5a) indicated the diffusion coefficient varied as $\sim T^{a}$ where $a = 8 \pm 1$ (±s.d.). The rate of oxygen uptake could be fitted with a Boltzmann dependence $\exp(-\Delta G/k_B T)$, as suggested from several previous studies of metabolic rate dependence with temperature [33], whose effective free energy activation barrier, ΔG, we estimate as 18 ± 4 kcal/mol (±s.d.) where T is the absolute temperature and k_B the Boltzmann constant (Supplementary Figure 5b). Previous estimates from lipid vesicles suggest free energy barrier values corresponding to the phospholipid phase transition process greater than our observed value here by a factor of 2-3 [36], and so phospholipid phase transition behaviour *per se* is unlikely to account for the temperature dependence in our present study. Conversely, *in vitro* estimates from kinetic studies of isolated enzymes indicate that for each electron pair transferred in the oxidation of a

molecule of NADH there is a gain in free energy through the transmembrane protonmotive force of ~31 kcal/mol, sufficient to energize the synthesis of three molecules of ATP requiring ~22 kcal/mol. Similarly, the oxidation of a molecule of succinate results in an increase in free energy through the protonmotive force of ~20 kcal/mol, sufficient to energize synthesis of two molecules of ATP requiring ~15 kcal/mol [42]. Therefore, synthesis of ATP from NADH and succinate requires free energy coupled to the protonmotive force of ~15-22 kcal/mol, which agrees with our observed free energy barrier to within experimental error. It is therefore likely that ubiquinone is a significant mediator of electron flow acting as a common electron carrier between different membrane patches.

Our results also shed light on spatial organization of the *E. coli* chemiosmotic proton circuit. We tagged two of the major sites for pmf generation, NADH:ubiquinone oxidoreductase and cytochrome bd-I, and one of the major sinks for the pmf, F_oF_1ATPase. The lack of any co-localization between NDH-1 and cytochrome bd-I indicates that pmf is generated by different complexes at multiple sites in the membrane. Likewise, the lack of co-localization between cytochrome bd-I and F_oF_1ATPase (Fig. 1d middle panel) indicates that sinks for the pmf are not necessarily located close to pmf sources. We also note that another pmf sink, the flagellar motor, is dispersed around the cell surface and immobilized by association with the cell wall [43], so unlikely to co-localize significantly with patches of NADH:ubiquinone oxidoreductase, cytochrome bd-I and F_oF_1ATPase that we observe. It has been suggested that pmf in chemiosmotic membranes may be effectively localized by binding of protons to lipid head-groups, and this localization is energetically advantageous if the pmf sink is located close to the pmf

source [44]. However, our results indicate that in *E. coli* the pmf is utilized by complexes spatially separated from pmf sources, therefore the classical picture of pmf delocalized over the entire cell surface is more likely.

The localization of these *E. coli* OXPHOS complexes contrast strikingly with the emerging picture of the inner mitochondrial membrane, where functional electron transport supercomplexes seem to play significant roles [11,45], and F_oF_1ATPase is located in a spatially-controlled fashion at cristae margins [46]. A key to the different strategies employed in *E. coli* and mitochondria may lie in the need for *E. coli* to rapidly acclimatize to changing environments by regulating expression of multiple electron transport modules. Such flexibility would be difficult to achieve if enzymes were locked into stable supercomplexes. By contrast, mitochondria inhabit a more stable environment in eukaryotic cytoplasm, exhibiting very restricted electron transport options, which may indicate a distinct adaptation. Supercomplexes may have evolved stochastically at the level of associations between individual pairs of OXPHOS enzymes, as opposed to *en masse*, which may explain the observation of supercomplexes in *E. coli* from other studies [35,47]and for other bacteria such as *Paracoccus denitrificans* [8]. Interestingly, recent data from fluorescence imaging and immuno EM of native mitochondrial OXPHOS enzymes suggest that the formation of supercomplexes may be a slow, stochastic process mediated by restricted diffusion in the cristae [48], and data from photosynthetic cyanobacteria also suggest a pooling of electron transport complexes into membranes patches of diameter 100-300nm [49].

Our results belong to a rapidly emerging field of single-molecule cellular biophysics [50], and although restricted to *E. coli* may suggest deeper reflection on the

physiological role OXPHOS supercomplexes. In addition, the presence of distinct patches whose size and mobility are heterogeneous, may indicate a general level of local membrane architecture beyond the OXPHOS process, with more complexity than has been assumed in prokaryotes.

Materials and Methods

Cell strain construction and characterization

Mutagenesis of E. coli strains

I) λ -red mediated recombination using the nptI-sacB (kanamycin-sucrose) counterselection. The relevant endogenous OXPHOS genes were replaced with functional fluorescent protein fusions performed through λ -red mediated recombination [51,52] allowing integration of either the *egfp* or *mcherry* gene coding for enhanced GFP or mCherry respectively [53,54] into the chromosomal operon for the *E. coli cyd-*, *cyo*, *atp*, *nuo-* and *sdh-* genes respectively. In brief, plasmid pKF2-6 contained all the genes for *E. coli* F_oF_1-ATP synthase and additionally coded for a fusion of eGFP to AtpB (*atpB*) at the C-terminus. To integrate into the chromosome we inserted the *nptI-sacRB* cartridge in the genomic operon, replacing *atpB*, via λ–red mediated recombination. The cartridge was amplified from plasmid pVO1100 using primers P18 and P19 (Supplementary Table S2) that imparted flanking homologous regions to the chromosomal *atp*-operon and this new BW25113 *atpB::nptI-sacRB* strain was characterized by colony PCR. For the insertion of the genes for the fluorescently-labelled subunit AtpB we amplified a linear fragment from pkF2-6 with primers P20 and P21 (Supplementary Table S2). The fragment was integrated into the chromosome of

BW25113 *atpB::nptI-sacRB* via λ-red mediated recombination. The strain BW25113 *atpB-egfp* was characterized by colony PCR and by sequencing. BW25113 *egfp-nuof,* BW25113 *sdhc-mCherry* and BW25113 *cyoA-mcherry* were similarly produced. The NuoF-GFP:SdhC-mCherry dual-labelled strain was made using the same methods.

II) Combination λ -red mediated recombination and double-strand break repair. Strains expressing the CydB-mCherry fusion protein were made by introducing the mCherry DNA coding sequence into the *E. coli* genome, downstream of *cydB* with the same 5 amino acid linker used in the construction of strain YTL01 [14]. This was achieved by a modification of the method previously described based on λ-red recombination and DNA double-stranded break repair [55]. Briefly, the pTKS/CS and pTKIP plasmids were replaced by plasmids pTKYTLmCh(v) and pYTLmChDonor. In pTKYTLmCh(v) the random sequence 'landing pads' from pTKS/CS were replaced with 30 base sequences with homology to the N and C termini of mCherry, to form 'landing pads' for mCherry. The neomycin resistance cassette in pTKIP-neo was replaced with the mCherry coding sequence to yield pYTLmChDonor. The red recombination plasmid pTKRED, was introduced into host strains by electroporation. Overlap PCR was used to generate the recombineering template which consisted of 2-300 bases of homology to the C-terminus of CydB, the 5 amino-acid linker coding sequence, N-terminal mCherry landing pad, the tetA counter-selectable marker with flanking I-SceI restriction sites, C-terminal mCherry landing pad and 2-300 bases of downstream homology to CydB. The introduction of the counter-selectable marker into the host strain genome and at its subsequent replacement with mCherry was carried out accordingly [55], using pYTLmChDonor in place of

pTKIP-neo. Mutants were screened by colony PCR and subsequent sequence analysis of the *cydB* allele in mutant colonies. The *cydB-mCherry* allele was similarly introduced into BW25113 *egfp-nuoF* and BW25113 *atpB-egfp*.

III) λ -red mediated recombination using nptI-ccdB (kanamycin-rhamnose) counterselection. *E. coli* strains expressing mMaple [22] tagged CydB and NuoF were generated by allele replacement on the *E. coli* MG1655 chromosome by λ-Red Recombination with λ-Red plasmid pTKRED [55]. Two rounds of recombination were used to achieve the desired mutation. In the first round of recombination, the recombination templates were generated by PCR amplification of the counter-selectable cassette from plasmid pKD45 [56], encoding kanamycin resistance and the *ccdB* toxin under the control of the rhamnose inducible *rha* promoter, using primer pair *cydB*-cs-F and *cydb*-cs-R, for mutations of the *cyd* operon, and primers *nuof-cs-F* and *nuoF-cs-R,* for mutations to the *nuo* operon (primer sequences are given in Supplementary Table S2). This counter-selection was deemed to be the most efficient hence the use of MG1655 rather than BW25113, which has a *Δrha* genotype [51] and therefore can neither import nor metabolize rhamnose. Using these templates, the counter-selectable cassette was inserted into the *cyd* and *nuo* operons at the insertion sites for the *mMaple* gene by λ-Red Recombination with λ-Red plasmid pTKRED as previously described [55]. Recombinants were selected by growth at 30 °C on LB plates with kanamycin (50 μg/ml) and spectinomycin (100 μg/ml) yielding mutants resistant to kanamycin but sensitive to rhamnose. In the second round of λ-Red Recombination, primer pairs *cydB-maple*-F and *cydB-maple*-R and *nuoF-maple*-F and *nuoF-maple*-R were used to PCR amplify the

mMaple gene and linker with flanking homology to the insertion sites in the *cyd* and *nuo* operons respectively. λ-Red Recombination was performed as before with these new templates and second-round recombinants were selected for by growth on M9 minimal medium plates with 0.3% rhamnose as the sole carbon source. The counter-selectable cassette was thus replaced with the *mMaple* gene. The primary sequences of the linkers used were identical to those for mCherry tagging of CydB and GFP tagging of NuoF. Mutants were confirmed by colony PCR and sequencing of the mutant alleles.

Characterization of E. coli strains

These cell strains were confirmed as having similar cell doubling-time measurements when grown in rich Luria-Bertani (LB) medium as the parental strain BW25113, with western blotting of the detergent-extracted cytoplasmic membrane content confirming the presence of fluorescent protein fusion constructs at the correct anticipated molecular weights. OXPHOS activity was estimated to be at least ~70% of the parental strain level, either from measuring NADH or succinate oxidase activity of cytoplasmic membranes and either NADH/ferricyanide oxidoreductase activity of cytoplasmic membranes and detergent extracts for the complex I or II variants respectively, or with estimating ATP-synthase activity of the *atpB-egfp* cell strain using succinate minimal media plates [18].

Fluorescence imaging of CydB-mCherry expressing strains showed red fluorescence localized to the periphery of the cell, indicating that the fusion protein is expressed, and that it remains intact. By phenotypic tests described for a previous cydB-GFP fusion strain [14], CydB-mCherry was determined to be a functional protein.

The aerobic growth of single- and dual-label strains in batch cultures was compared to the parental wild-type strain BW25113, with measured cell doubling times under aerobic growth for all strains used shown in Supplementary Table S1. Function of the CydB-mMaple expressing strain was demonstrated by comparison of growth of this strain with wild-type and *cydB*-knockout strains.

Synthesis of fluorescently labelled ubiquinone

NBDHA-Q was synthesized, modifying a previous protocol [57,58].

General methods and chemical instrumentation:

Commercially available reagents were used as received without further purification. All reactions required anhydrous conditions and were conducted in flame-dried apparatus under an atmosphere of nitrogen. Analytical thin-layer chromatography (TLC) was performed on silica gel plates (0.25 mm) pre-coated with a fluorescent indicator. Standard flash chromatography procedures were performed using Kieselgel 60 (40-63 μm). UV/Vis spectra were recorded using a PerkinElmer Lambda 35 UV/Vis spectrometer. ^{1}H NMR spectra were recorded using a Bruker AV400 NMR spectrometer. Chemical shifts δ are reported in ppm (relative to TMS (δ_H = 0.0) and multiplicity of signals denoted s = singlet, bs = broad singlet, d = doublet, t = triplet, m = multiplet respectively with coupling constants (*J*) reported in Hertz (Hz).

Preparation of NBD-idebenone (3):

To a solution of 6-aminohexanoic acid (263 mg, 2.00 mmol) and $NaHCO_3$ (506 mg, 6.00 mmol) in MeOH (20 mL) at 0 °C was added 4-chloro-7-nitrobenzofurazan

(NBD-Cl) (401 mg, 2.00 mmol) portion-wise. The reaction was stirred at 50 °C for 2 h before being cooled and acidified by careful addition of dilute HCl (0.1 M). The precipitate was filtered off and then purified by flash column chromatography (SiO_2; $CHCl_3 \rightarrow$ 2% MeOH in $CHCl_3$) and then by recrystallization from MeOH/H_2O to give 6-(7-nitrobenzo[*c*][1,2,5]oxadiazol-4-ylamino)hexanoic acid (100 mg) as an orange solid (100 mg); ^{1}H NMR (DMSO-d_6) δ = 11.98 (bs, 1H), 9.53 (bs, 1H), 8.51 (d, *J* = 8.6 Hz, 1H), 6.41 (d, *J* = 8.6 Hz, 1H), 3.51-3.42 (m, 2H), 2.22 (t, *J* = 7.3 Hz, 2H), 1.73-1.64 (m, 2H), 1.61-1.49 (m, 2H), 1.42-1.32 (m, 2H).

To a solution of (100 mg, 0.34 mmol, 3.4 equiv.) in anhydrous CH_2Cl_2 (5 ml) under N_2 was added *N*,*N*′-dicyclohexylcarbodiimide (DCC) (37 mg, 0.18 mmol, 1.8 equiv.) in a reaction vessel shielded from UV light. The reaction was left to stir at room temperature for 5 h at which point the orange solid had fully dissolved and a white precipitate (dicyclohexylurea) was visible. 4-(Dimethylamino)pyridine (DMAP) (1.0 mg, 0.2 µmol, 2.0 x10^{-3} equiv.) and idebenone (35 mg, 0.1 mmol, 1.0 equiv.) were then added and the reaction was left to stir for a further 16h. The reaction mixture was then filtered and concentrated under reduced pressure at room temperature, before purification of the red/orange residue by silica gel chromatography (*n*Hexane:EtOAc; 1:1) limiting UV exposure to a minimum afforded the title compound as a bright orange solid (20.9 mg, 34.0%). R_f = 0.27; ^{1}H NMR (400 MHz, $CDCl_3$): δ = 1.03-1.93 (m, 16 H, 8 x CH_2), 1.97 (s, 3H, CH_3), 2.39 (t, 2H, *J* = 6.7 Hz, CH_2), 3.43-3.51 (m, 2H, CH_2), 3.57-3.68 (m, 2H, CH_2), 3.85-3.96 (m, 2H, CH_2), 4.01 (s, 6H, 2 x OCH_3), 6.10 (d, 1H, *J* = 8.6,

CH ß to NO_2), 6.71 (brs, 1H, NH), 8.40 (d, 1H, J = 8.6, CH α to NO_2); UV_{max} (EtOH) = 463.

Microscopy

For near-TIRF imaging [59] we used a home-built inverted dual-color microscope capable of multi-modal illumination, including controlled near-TIRF/TIRF microscopy, providing laser excitation at 473 nm and 561 nm wavelengths for GFP and mCherry respectively at intensities in the range 125-250 W cm^{-2}. Emissions were separated into green/red channels using a bespoke spectral splitter and imaged at 25 Hz onto separate halves of a 512x512pixel, cooled, back-thinned EMCCD camera (iXon+ DV897-BI, Andor Technology, UK) at a magnification of ~40 nm/pixel, sampling continuously for up to ~10 s.

We set the focal plane at 100 nm from the glass coverslip surface, to image cytoplasmic membranes of single *E. coli* cells [43]. With near-TIRF, the angle of laser incidence was sub-critical at ~45° resulting in oblique transmission into the sample. We obtained high contrast due to reduction in back-scatter, but resulting in uniform excitation across individual cells unlike conventional TIRF. The objective lens depth of field was low (0.2 μm) compared to *E. coli* cell diameters (1 μm), resulting in relatively planar imaged sections with little correction required for membrane curvature.

PALM imaging

Overnight cultures in LB were diluted 1:20 in M9 medium with glucose (0.2 %) as a carbon source and grown aerobically for 3-4 h to OD600 0.6-0.7 at approximately 30°C.

Cells pellets were obtained by centrifugation and washed in filtered growth medium and fixed in a solution of 4% paraformaldehyde, 0.1 % glutaraldehyde in phosphate buffered saline at approximately 30 °C for 15 min. Fixed cells and 100 nm gold nanospheres, used as fiducial markers, were adhered to poly-L-lysine coated cleaned coverslips by centrifugation in a microcentrifuge at 6000rpm for 1 min in coverslip-holder/chambers. Samples were rinsed with filtered media and imaged in a reservoir of medium.

Samples were imaged with TIRF illumination in a custom-built fluorescence microscope and images rendered as described previously [60]. Briefly, a 561 nm wavelength laser of intensity 22 $mWmm^{-2}$ was used to excite mMaple fluorophores in their red state and a 405 nm wavelength laser was used to switch fluorophores from their green to red state. The intensity of the 405 nm laser was continuously increased up to an intensity of 3.5 $mWmm^{-2}$ during acquisition in an approximation to a Fermi activation regime [60], minimizing the likelihood of simultaneous photoactivation of multiple molecules and thus optimally separating single molecules in time. Fluorescence was detected by an Andor iXon+ EMCCD camera sampling at 50 ms per frame using typically 8,000-10,000 consecutive image frames in total for PALM reconstruction. Image reconstruction was as previously reported [60]. The centres of cylindrical Gaussian distributions with standard deviation determined by the localization uncertainty of that molecule, calculated as previously described [61], and normalized integrated intensity were centred on localizations of mMaple. Bright patches are produced by the summation of multiple Gaussian profiles in close proximity to one another. Fields of view showing multiple cells are shown in Supplementary Figure 1.

NBDHA-Q-FRAP

FRAP experiments were performed using a Leica TCS-SP5 laser-scanning confocal microscopy with 63× oil-immersion objective (NA 1.4) and excitation wavelength 488 nm, recording emission at 515-560 nm.

Data analysis

Spatial shift between green and red channels during two-color imaging

The spatial shift between the green and red channels on the image plane, was determined for each image sequence by finding the position of best overlap of the two channels on the corresponding brightfield sequence (non-fluorescence images which bled through into each channel), acquired prior to each fluorescence sequence during data acquisition. This was done using a frame average (typically 10 frames) of the brightfield sequence, separating it into its red channel and green channel halves, calculating a spatial cross-correlation function of the top and bottom halves and finding the position of the maximum of that cross-correlation function on the image plane. This position corresponded to the spatial shift of the red channel with respect to the green one during image acquisition. This shift was typically up to a few pixels and could be due to alignment of the optics and to chromatic aberrations. Only a linear shift on the image plane was considered for our analysis.

Tracking software

Spots could be localized using bespoke software in MATLAB (Mathworks) improved from earlier algorithms [62]. This software recognized spots, quantified spot widths as well as corrected for local background intensity due to diffuse fluorescent protein, cellular autofluorescence or 'dark' camera noise.

Initially, an average of the first few frames (typically five) in a given image sequence was used to obtain, by means of image pixel-thresholding, a cell mask and a background mask, in order to distinguish the regions on the image where bacteria cells were actually located, from background regions. These cell masks were used for estimating cell length and width, as well as for transforming Cartesian coordinates of tracked spots to a local cell coordinate system referenced to the geometric centroid of the cell image.

Candidate positions for bright spots were found on each frame within a given image sequence by applying a combination of morphological image transformations. For candidate spots within the 'cell' region, an iterative Gaussian-masking algorithm [23,28,43] was used to locate the intensity centroid of the bright spots on the image plane with sub-pixel precision (<40 nm). This algorithm essentially finds the position of best overlap of the spot's intensity distribution with a two-dimensional Gaussian distribution of fixed width (sigma=2 pixels) which moves around within a fixed squared sub-array of edge length 17 pixels. Inside this sub-array, a circular region of diameter 10 pixels and centred on the determined spot centre position, was used to discriminate the bright spot from its surroundings.

The average background counts per pixel were calculated from the mean of the intensities in all pixels in the background region, i.e. the region within the fixed squared sub-array but outside the circular spot region. Background subtraction was then performed by subtracting this average background (per pixel) from the intensity corresponding to each pixel in the inner circular region. A final total spot intensity was calculated by adding all resulting intensities, after background subtraction, within this circular region. A Gaussian function was fitted to the resulting background-corrected total spot intensity in order to characterize all spots by obtaining their width and peak intensity.

A detected spot was accepted only if it had large enough signal-to-noise ratio (SNR) and *r*-squared value of the Gaussian fit, and a width below the diameter of the above mentioned inner circular region. The SNR was calculated as the peak intensity of the Gaussian fit of the spot divided by the standard deviation of all the intensities in the background region. The corresponding Gaussian fit for each candidate and accepted spot was subtracted from the raw frame data before attempting to find the next spot centre. This step improved the chances of detecting spots which were very close together, particularly for dim spots adjacent to much brighter spots.

Two accepted bright spots in consecutive frames were then linked into a track if, simultaneously, their centres were less than 5 pixels apart, the ratio of their widths was between 0.5 and 2, and the ratio of their background-corrected total spot intensities was between 0.5 and 3. When there were competing assignments with several bright spots that could be possibly linked to a spot in a previous frame, the best assignment was chosen such that the distance between the spot centres to link was minimized.

We generated simulated data in the form of synthetic image sequences with controlled background and shot noise levels and ran these through the algorithm finding a localization precision of <1 pixel (i.e. <40 nm).

Stoichiometry analysis:

For our stoichiometry calculations, we used the total fluorescence spot intensity (integrated over the whole spot), and corrected for any local background. No filtering of the data was employed. First, a photobleaching time constant was obtained for a given fluorophore (GFP or mCherry) and data set (at given excitation laser powers) by means of two different approaches. The first approach consisted of obtaining the intensity integrated over the whole bacteria cell body as a function of time, for each image sequence, and fitting it to an exponential decay function with no offset. This approach was consistent with the measured background cell autofluorescence contribution being negligible compared to the measured whole cell intensity due to either GFP or mCherry (the measured bleaching rate measured from the parental strains, without fluorescent protein labels, was significantly faster). The photobleaching time constants obtained in this way for all image sequences in a given data set were then used to determine a resulting range of values for the photobleaching time constant.

These determined time constant values were checked for consistency against a second method, which consisted of constructing an averaged intensity trace from many tracks from many spots within the data set. Tracks had their intensity normalized to the initial intensity at the start of the track, and their time origin was shifted so that they would all start at time zero before being averaged. Only tracks with at least 25 points

(~1s long) were used, and only points on the averaged trace resulting from an average over at least 2-5 tracks were kept. The error for each point on the averaged trace was calculated appropriately and used for weighting the exponential fitting of the resulting averaged trace. A final range of values for the photobleaching decay time constant was obtained combining the ranges of values obtained from the two methods outlined above, for every data set and for each fluorophore. The relative error in these final estimates was between 7% and 36% for the majority of the data sets, though very rarely as high as 50% for one data set.

The determined photobleaching time constants were then used as fixed parameters for fitting the intensities of all tracks from all images (for a given data set and fluorophore), to exponential fits with no offset. An estimate of the initial spot intensity at the start of the data acquisition was obtained from the fit. Only tracks with a minimum of 5 data points were fitted, and results from the exponential fits with pre-determined time constants were only accepted for positive *r*-squared values and for small enough squared deviations of the fitted model from the data points averaged over all data points. Also, a reduced chi-squared test was performed in order to assess the goodness of all fits imposing a probability level of 99% for acceptance.

The stoichiometry of each tracked bright spot was then determined by dividing the obtained initial intensity for each track by the corresponding single-molecule brightness value obtained from purified, immobilized single-molecule fluorescent proteins (Supplementary Figure 2). From all final stoichiometry values, a histogram or a Gaussian kernel distribution (a sum of many Gaussian curves, one per stoichiometry

value, centred on the stoichiometry value and with a Gaussian width equal to the uncertainty of that value) was derived.

The single-molecule fluorophore brightness (intensity) estimates from *in vitro* data were obtained by firstly detecting point spread function width (HWHM of 200-300 nm) spots of distinct fluorescence intensity on the frame averaged *in vitro* image sequences of single-molecule GFP or mCherry in a manner as described previously [20]. Traces of spot intensity versus time were then obtained for each fixed position of the bright spots found on the frame average. The intensity values were background corrected in the same way as for the previously described analysis of *in vivo* data.

Calculation of the overlap integral for co-localization analysis

Having two normalized, two-dimensional Gaussian intensity distributions g_1 and g_2, centred around (x_1, y_1) with width σ_1, and around (x_2, y_2) with width σ_2, respectively, and defined as:

$$g_1(x,y) = e^{-[(x-x_1)^2+(y-y_1)^2]/(2\sigma_1^2)},$$

$$g_2(x,y) = e^{-[(x-x_2)^2+(y-y_2)^2]/(2s_2^2)},$$

their overlap can be calculated from the integral of their product:

$$v_0 = \int_{-\infty-\infty}^{+\infty+\infty} g_1(x,y)g_2(x,y)dxdy = Ce^{-\Delta r^2/[2(\sigma_1^2+\sigma_2^2)]}.$$

Here, Δr is the distance between the centres of the Gaussians on the *x*-*y* image plane, and *C* is a normalization constant equal to the maximum overlap possible for two perfectly overlapped spots of different widths σ_1 and σ_2, so that:

$$\Delta r^2 = (x_1 - x_2)^2 + (y_1 - y_2)^2,$$

$$C = \frac{2\pi\sigma_1^{\,2}\sigma_2^{\,2}}{\sigma_1^{\,2}+\sigma_2^{\,2}}.$$

We defined the overlap integral, *v*, for a pair of spots of known positions and widths as:

$$v = \frac{v_0}{C} = e^{-\Delta r^2/[2(\sigma_1^2+\sigma_2^2)]}.$$

Calculating the likelihood for random chance co-localization of OXPHOS fluorescent spots

Using nearest neighbour analysis for a random distribution of particles on a two-dimensional surface - a modification of the analysis presented in [63] for three dimensions - we can call $p(r)dr$ the probability that the distance from one OXPHOS fluorescent spot in the cell membrane to another of the same type in a given single-label cell strain is between r and $r+dr$. This must be equal to the probability that there are zero such fluorescent spots particles in the range 0-r, multiplied by the probability that a single spot exists in the annulus zone between r and $r+dr$. Thus:

$$p(r)dr = \left[1 - \int_0^r p(r')dr'\right] 2\pi r n dr$$

Here, n is the number of bright spots per unit area in the patch of cell membrane observed in the focal plane under near-TIRF imaging. This indicates that:

$$\frac{d}{dr}\left(\frac{p}{2\pi r n}\right) + 2\pi r n \cdot \frac{p}{2\pi r n} = 0$$

Solving for $p(r)$ and using that $p \to 2\pi r n$ in the limit $r \to 0$, we obtain:

$$p(r) = 2\pi r n \exp\left(-\pi r^2 n\right)$$

Thus, the probability $p_1(w)$ that the nearest neighbour spot separation is greater than a distance w is [59]:

$$p_1(w) = 1 - \int_0^w p(r)dr = 1 - \int_0^w 2\pi rn \exp(-\pi r^2 n)dr = \exp\left(-\pi w^2 n\right)$$

The effective number density per unit area, n, at the focal plane is given by the number of spots N_{mem} observed in the cell membrane (N_{mem} ~4 spots per image on average over all cell strains: 2 spots in each channel, i.e., 2 mCherry-labelled plus 2 GFP-labelled OXPHOS complexes), divided by the portion, A, of the *E. coli* cell membrane imaged in focus within the 0.2 μm depth of field of our microscope's objective lens using near-TIRF illumination. Assuming each cell can be approximated by a cylinder capped with hemispheres of total length ~3 μm and diameter ~1 μm, we estimate that approximately a quarter of the total surface cell membrane area of the bacteria is within 200nm of the coverslip and imaged in focus (the focal plane was set at ~100 nm from the glass coverslip). Therefore A~2.5 μm^2 (the total bacterial membrane area would be ~9 μm^2 or ~ 6,000 $pixels^2$ on our camera detector).

The probability that a nearest neighbour spot will be a distance less than w away is given by $1-p_1(w) = 1-\exp(-\pi w^2 N_{\text{mem}}/A)$. If w is set to be the optical resolution limit (w_{res}~0.3 μm, equivalent to ~6 pixels on our camera detector) then we obtain a value $1-p_1(w_{res})=0.37$. The probability of chance co-localization of two spots of different types (different OXPHOS complexes) is 2/3 of that value, i.e. 0.24. Therefore, the probability of chance co-localization of different OXPHOS complexes within the optical resolution limit of our microscope is $p_{\text{chance}} \approx 24\%$.

Note that we have made sure that bleed-through from one channel (color) into the other was negligible. Additionally, possible spontaneous spectral shifts due to changes in the cell environment (in the fluorophore neighbourhood) are small, of order ~20-30nm [25,64]. In our experiments, GFP and mCherry fluorophores are excited at laser wavelengths of 473nm and 561nm, respectively, which are ~90nm apart. Our excitation filters are ~20nm wide, and so are our emission filters, for which the central wavelengths are also ~90nm apart. Hence, possible small spectral shifts could not be responsible for 'false positives' of co-localisation.

Comparison to other reported methods for co-localization analysis

Alternative popular recent methods of co-localization analysis are image cross-correlation spectroscopy (ICCS) [65] and standard fluorescence microscopy co-localization algorithms such as Pearson's coefficient and Manders' coefficients M1 and M2 [66]. Pearson's coefficient only performs well for samples with similar stoichiometries (number densities) of fluorescently labelled complexes in each channel, and the method based on Manders' coefficients works well for number density ratios up to ~2, being very sensitive to the choice of the relevant required thresholds which can in turn be determined through automatic algorithms [67]. Both Pearson's and Manders' coefficient methods work better at low particle densities and are more sensitive than ICCS, being capable of measuring low levels of co-localization. ICCS performs better at high number densities and is more accurate when the particle densities in the two channels are different (density ratios up to ~10). However, ICCS fails for low co-

localization fractions and is particularly sensitive to image heterogeneity, since a step involving fitting a spatial correlation function to a Gaussian can become non-trivial for images in which the spatial distribution of bright particles is not sufficiently uniform (for instance, images with sharp bright edges such as cell boundaries), making the automation of this step technically challenging, and hence making the ICCS method unusable in a practical context.

Given the very different stoichiometries of the labelled complexes in our red and green channels, the low level of co-localization seen on our image sequences, and the heterogeneity of our fluorescence images here, we use 'co-localization value' maps and estimate co-localization fractions by use of overlap integrals. Our calculation of overlap integrals is similar to that described previously [28], but improves the algorithm by employing a Rayleigh-type criterion to determine a co-localization threshold, where histograms of displacements on the image plane of putatively co-localized spots are plotted and fitted to a 2D Gaussian function using three times the Gaussian width as a fixed threshold to determine co-localization fractions. The authors have recently become aware of a similar approach to ours in recent work [68] However, our method is more generic and includes the possibility of considering variable spot widths in the two channels when calculating the overlap integral.

Mobility analysis

The Bayesian Ranking of Diffusion (BARD) analysis inputs spatial *x*-*y* coordinates for each detected spot as a function of time over which is it is tracked, and constructs an estimate for the theoretical *posterior* distribution corresponding to common diffusion

modes of anomalous/sub-diffusion, normal/Brownian, confined, or directed diffusion by using the measured mean square displacement (*MSD*) of each track in combination with analytical *prior* distributions which indicate the expectations of mobility parameters. The *MSD* for anomalous, Brownian and directed diffusion was modelled as:

$$MSD = 4D\tau^{\alpha} + v\tau^{2},$$

where D is the apparent diffusion coefficient, τ the time interval, α the anomalous diffusion coefficient (set to precisely 1 for Brownian, and 0.7-0.8 for anomalous diffusion) and v is the mean drift-speed (set to precisely zero for Brownian and anomalous diffusion models). For confined diffusion, a circularly symmetrical confinement domain was modelled in which Brownian diffusion could occur inside the domain subject to a harmonic potential well such that a particle at the domain edge experiences a forcing function that drives it back into the domain [25].

The calculated posteriors were then ranked from lowest to highest probability, with highest corresponding to the most likely model accounting for the observed data. Relevant mobility parameters for each diffusion mode, for example the diffusion coefficient and the equivalent radius of a confinement domain, could then be extracted for each track.

The performance of the BARD algorithm was characterized thoroughly using multiple simulated 2D tracks of particles covering a broad range of effective diffusion coefficients and confinement radii, as well as other mobility parameters such as mean drift speed and anomalous diffusion coefficient, as outlined in full in [25]. Simulating purely immobile particles, i.e. with a zero effective diffusion coefficient, but with a

realistic Gaussian noise on spatial localization equivalent to the high end of the experimental localization precision for a single GFP molecule under our imaging conditions of sigma width ~40 nm, indicated that the most likely diffusion model from the four candidates models used above was confined with a predicated confinement radius of 15 ± 10 nm. Brighter diffusing particles, e.g. equivalent to the intensity of 10-100 fluorescent protein molecules as found from our experimental OXPHOS data, have a smaller localization precision by roughly the square-root of this increase in brightness factor [61], consistent with our simulations indicating a range of localization precision of ~5-30 nm across the range of spot intensities we observed experimentally, indicating a predicted confinement radius for simulated immobile particles of more typically ~5 nm.

Respiratory rate analysis

Oxygen uptake of *E. coli* cultures at defined temperatures was measured in a Hansatech Oxylab electrode, with water-jacketed electrode chamber for temperature control.

References

[1] P. Mitchell, Coupling of phosphorylation to electron and hydrogen transfer by a chemi-osmotic type of mechanism, Nature. 191 (1961) 144–148.

[2] P.R. Rich, The molecular machinery of Keilin's respiratory chain, Biochem. Soc. Trans. 31 (2003) 1095–1105.

[3] G. Unden, J. Bongaerts, Alternative respiratory pathways of Escherichia coli: energetics and transcriptional regulation in response to electron acceptors, Acta-Bioenerg. 1320 (1997) 217–234.

[4] G. Lenaz, M.L. Genova, Kinetics of integrated electron transfer in the mitochondrial respiratory chain: random collisions vs. solid state electron channeling, Am J Physiol Cell Physiol. 292 (2007) C1221–39.

[5] B. Chance, G.R. Williams, A method for the localization of sites for oxidative phosphorylation, Nature. 176 (1955) 250–254.
[6] H. Schägger, K. Pfeiffer, Supercomplexes in the respiratory chains of yeast and mammalian mitochondria, Embo J. 19 (2000) 1777–1783.
[7] C.M. Cruciat, S. Brunner, F. Baumann, W. Neupert, R.A. Stuart, The cytochrome bc1 and cytochrome c oxidase complexes associate to form a single supracomplex in yeast mitochondria, J Biol Chem. 275 (2000) 18093–18098.
[8] A. Stroh, O. Anderka, K. Pfeiffer, T. Yagi, M. Finel, B. Ludwig, et al., Assembly of respiratory complexes I, III, and IV into NADH oxidase supercomplex stabilizes complex I in *Paracoccus denitrificans*, J Biol Chem. 279 (2004) 5000–5007.
[9] M. Zhang, E. Mileykovskaya, W. Dowhan, Cardiolipin is essential for organization of complexes III and IV into a supercomplex in intact yeast mitochondria, J Biol Chem. 280 (2005) 29403–29408.
[10] E. Nübel, I. Wittig, S. Kerscher, U. Brandt, H. Schägger, Two-dimensional native electrophoretic analysis of respiratory supercomplexes from Yarrowia lipolytica, Proteomics. 9 (2009) 2408–2418.
[11] N.V. Dudkina, J. Heinemeyer, S. Sunderhaus, E.J. Boekema, H.-P. Braun, Respiratory chain supercomplexes in the plant mitochondrial membrane, Trends Plant Sci. 11 (2006) 232–240.
[12] E. Schäfer, H. Seelert, N.H. Reifschneider, F. Krause, N.A. Dencher, J. Vonck, Architecture of active mammalian respiratory chain supercomplexes, J Biol Chem. 281 (2006) 15370–15375.
[13] A.S. Johnson, S. van Horck, P.J. Lewis, Dynamic localization of membrane proteins in Bacillus subtilis, Microbiology. 150 (2004) 2815–2824.
[14] T. Lenn, M.C. Leake, C.W. Mullineaux, Clustering and dynamics of cytochrome bd-I complexes in the Escherichia coli plasma membrane in vivo, Mol. Microbiol. 70 (2008) 1397–1407.
[15] M. Renz, T. Rendler, M. Börsch, Diffusion properties of single FoF1-ATP synthases in a living bacterium unraveled by localization microscopy, (2012) 822513–822513–11.
[16] T. Appelhans, C.P. Richter, V. Wilkens, S.T. Hess, J. Piehler, K.B. Busch, Nanoscale organization of mitochondrial microcompartments revealed by combining tracking and localization microscopy, Nano Lett. 12 (2012) 610–616.
[17] T. Lenn, M.C. Leake, C.W. Mullineaux, Are Escherichia coli OXPHOS complexes concentrated in specialized zones within the plasma membrane? Biochem. Soc. Trans. 36 (2008) 1032–1036.
[18] H. Erhardt, F. Dempwolff, M. Pfreundschuh, M. Riehle, C. Schäfer, T. Pohl, et al., Organization of the Escherichia coli aerobic enzyme complexes of oxidative phosphorylation in dynamic domains within the cytoplasmic membrane, MicrobiologyOpen. (Accepted 7 Jan 2014).
[19] B. Cui, C. Wu, L. Chen, A. Ramirez, E.L. Bearer, W.-P. Li, et al., One at a time, live tracking of NGF axonal transport using quantum dots, Proc Natl Acad Sci U S A. 104 (2007) 13666–13671.

[20] A. Badrinarayanan, R. Reyes-Lamothe, S. Uphoff, M.C. Leake, D.J. Sherratt, In vivo architecture and action of bacterial structural maintenance of chromosome proteins, Science. 338 (2012) 528–531.
[21] B. Huang, M. Bates, X. Zhuang, Super-resolution fluorescence microscopy, Annu Rev Biochem. 78 (2009) 993–1016.
[22] A.L. McEvoy, H. Hoi, M. Bates, E. Platonova, P.J. Cranfill, M.A. Baird, et al., mMaple: a photoconvertible fluorescent protein for use in multiple imaging modalities, PLoS One. 7 (2012) e51314.
[23] R. Reyes-Lamothe, D.J. Sherratt, M.C. Leake, Stoichiometry and architecture of active DNA replication machinery in Escherichia coli, Science. 328 (2010) 498–501.
[24] Y. Taniguchi, P.J. Choi, G.-W. Li, H. Chen, M. Babu, J. Hearn, et al., Quantifying E. coli proteome and transcriptome with single-molecule sensitivity in single cells, Science. 329 (2010) 533–538.
[25] A. Robson, K. Burrage, M.C. Leake, Inferring diffusion in single live cells at the single-molecule level, Philos Trans R Soc Lond B Biol Sci. 368 (2013) 20120029.
[26] S. Wieser, G.J. Schutz, M.E. Cooper, Single molecule diffusion analysis on cellular nanotubules: Implications on plasma membrane structure below the diffraction limit, Applied Physics …. (2007).
[27] M. Renner, Y. Domanov, F. Sandrin, I. Izeddin, P. Bassereau, A. Triller, Lateral diffusion on tubular membranes: quantification of measurements bias, PLoS One. 6 (2011) e25731.
[28] I.E.G. Morrison, I. Karakikes, R.E. Barber, N. Fernández, R.J. Cherry, Detecting and quantifying colocalization of cell surface molecules by single particle fluorescence imaging, Biophys J. 85 (2003) 4110–4121.
[29] B. Chazotte, E.S. Wu, C.R. Hackenbrock, The mobility of a fluorescent ubiquinone in model lipid membranes. Relevance to mitochondrial electron transport, Biochim Biophys Acta. 1058 (1991) 400–409.
[30] E. Boye, A. Løbner-Olesen, Bacterial growth control studied by flow cytometry, Res Microbiol. 142 (1991) 131–135.
[31] I. Fishov, C.L. Woldringh, Visualization of membrane domains in Escherichia coli, Mol. Microbiol. 32 (1999) 1166–1172.
[32] H. Kirchhoff, S. Haferkamp, J.F. Allen, D.B.A. Epstein, C.W. Mullineaux, Protein diffusion and macromolecular crowding in thylakoid membranes, Plant Physiol. 146 (2008) 1571–1578.
[33] J.F. Gillooly, J.H. Brown, G.B. West, V.M. Savage, E.L. Charnov, Effects of size and temperature on metabolic rate, Science. 293 (2001) 2248–2251.
[34] E.A. Berry, B.L. Trumpower, Isolation of ubiquinol oxidase from Paracoccus denitrificans and resolution into cytochrome bc1 and cytochrome c-aa3 complexes, J Biol Chem. 260 (1985) 2458–2467.
[35] P.M.F. Sousa, S.T.N. Silva, B.L. Hood, N. Charro, J.N. Carita, F. Vaz, et al., Supramolecular organizations in the aerobic respiratory chain of Escherichia coli, Biochimie. 93 (2011) 418–425.
[36] P. Cicuta, S.L. Keller, S.L. Veatch, Diffusion of liquid domains in lipid bilayer membranes, J Phys Chem B. 111 (2007) 3328–3331.

[37] S.L. Veatch, P. Cicuta, P. Sengupta, A. Honerkamp-Smith, D. Holowka, B. Baird, Critical fluctuations in plasma membrane vesicles, ACS Chem Biol. 3 (2008) 287–293.
[38] E.J. Deeds, O. Ashenberg, J. Gerardin, E.I. Shakhnovich, Robust protein protein interactions in crowded cellular environments, Proc Natl Acad Sci U S A. 104 (2007) 14952–14957.
[39] R.N. Frese, J.C. Pàmies, J.D. Olsen, S. Bahatyrova, C.D. van der Weij-de Wit, T.J. Aartsma, et al., Protein shape and crowding drive domain formation and curvature in biological membranes, Biophys J. 94 (2008) 640–647.
[40] N. Wilke, B. Maggio, The influence of domain crowding on the lateral diffusion of ceramide-enriched domains in a sphingomyelin monolayer, J Phys Chem B. 113 (2009) 12844–12851.
[41] S. Shalel-Levanon, K.-Y. San, G.N. Bennett, Effect of oxygen, and ArcA and FNR regulators on the expression of genes related to the electron transfer chain and the TCA cycle in Escherichia coli, Metabolic Engineering. 7 (2005) 364–374.
[42] H.F. Lodish, Molecular cell biology, 4 ed., W.H. Freeman, New York, 2000.
[43] M.C. Leake, J.H. Chandler, G.H. Wadhams, F. Bai, R.M. Berry, J.P. Armitage, Stoichiometry and turnover in single, functioning membrane protein complexes, Nature. 443 (2006) 355–358.
[44] D.A. Cherepanov, B.A. Feniouk, W. Junge, A.Y. Mulkidjanian, Low dielectric permittivity of water at the membrane interface: effect on the energy coupling mechanism in biological membranes, Biophys J. 85 (2003) 1307.
[45] E. Lapuente-Brun, R. Moreno-Loshuertos, R. Acín-Pérez, A. Latorre-Pellicer, C. Colás, E. Balsa, et al., Supercomplex assembly determines electron flux in the mitochondrial electron transport chain, Science. 340 (2013) 1567–1570.
[46] G.B. John, Y. Shang, L. Li, C. Renken, C.A. Mannella, J.M.L. Selker, et al., The mitochondrial inner membrane protein mitofilin controls cristae morphology, Mol Biol Cell. 16 (2005) 1543–1554.
[47] P.M.F. Sousa, M.A.M. Videira, A. Bohn, B.L. Hood, T.P. Conrads, L.F. Goulao, et al., The aerobic respiratory chain of Escherichia coli: from genes to supercomplexes, Microbiology. 158 (2012) 2408–2418.
[48] V. Wilkens, W. Kohl, K. Busch, Restricted diffusion of OXPHOS complexes in dynamic mitochondria delays their exchange between cristae and engenders a transitory mosaic distribution, J Cell Sci. 126 (2013) 103–116.
[49] L.-N. Liu, S.J. Bryan, F. Huang, J. Yu, P.J. Nixon, P.R. Rich, et al., Control of electron transport routes through redox-regulated redistribution of respiratory complexes, Proc Natl Acad Sci U S A. 109 (2012) 11431–11436.
[50] T. Lenn, M.C. Leake, Experimental approaches for addressing fundamental biological questions in living, functioning cells with single molecule precision, Open Biol. 2 (2012) 120090.
[51] K.A. Datsenko, B.L. Wanner, One-step inactivation of chromosomal genes in Escherichia coli K-12 using PCR products, Proc Natl Acad Sci U S A. 97 (2000) 6640–6645.

[52] T. Pohl, M. Uhlmann, M. Kaufenstein, T. Friedrich, Lambda Red-Mediated Mutagenesis and Efficient Large Scale Affinity Purification of the Escherichia coli NADH:Ubiquinone Oxidoreductase (Complex I)†, Biochemistry. 46 (2007) 10694–10702.

[53] Y. Ito, M. Suzuki, Y. Husimi, A novel mutant of green fluorescent protein with enhanced sensitivity for microanalysis at 488 nm excitation, Biochem. Biophys. Res. Commun. 264 (1999) 556–560.

[54] N.C. Shaner, R.E. Campbell, P.A. Steinbach, B.N.G. Giepmans, A.E. Palmer, R.Y. Tsien, Improved monomeric red, orange and yellow fluorescent proteins derived from Discosoma sp. red fluorescent protein, Nature Biotechnology. 22 (2004) 1567–1572.

[55] T.E. Kuhlman, E.C. Cox, Site-specific chromosomal integration of large synthetic constructs, Nucleic Acids Res. 38 (2010) e92.

[56] T. Kolmsee, R. Hengge, Rare codons play a positive role in the expression of the stationary phase sigma factor RpoS (σS) in Escherichia coli, RNA Biology. (2011).

[57] C.A. Yu, L.Q. Gu, Y.Z. Lin, L. Yu, Effect of alkyl side chain variation on the electron-transfer activity of ubiquinone derivatives, Biochemistry. 24 (1985) 3897–3902.

[58] J. Novotný, K. Pospechová, A. Hrabálek, R. Cáp, K. Vávrová, Synthesis of fluorescent C24-ceramide: evidence for acyl chain length dependent differences in penetration of exogenous NBD-ceramides into human skin, Bioorg. Med. Chem. Lett. 19 (2009) 6975–6977.

[59] G.J. Schutz, M. Sonnleitner, H. Schindler, Ultrasensitive microscopy of the plasma membrane of living cells, Journal of Fluorescence. 11 (2001) 177–185.

[60] S.-H. Lee, J.Y. Shin, A. Lee, C. Bustamante, Counting single photoactivatable fluorescent molecules by photoactivated localization microscopy (PALM), Proc Natl Acad Sci U S A. 109 (2012) 17436–17441.

[61] R.E. Thompson, D.R. Larson, W.W. Webb, Precise nanometer localization analysis for individual fluorescent probes, Biophys J. (2002).

[62] M.C. Leake, N.P. Greene, R.M. Godun, T. Granjon, G. Buchanan, S. Chen, et al., Variable stoichiometry of the TatA component of the twin-arginine protein transport system observed by in vivo single-molecule imaging, Proc Natl Acad Sci U S A. 105 (2008) 15376–15381.

[63] S. Chandrasekhar, Stochastic problems in physics and astronomy, Reviews of Modern Physics. 15 (1943) 0001–0089.

[64] M.A. Rizzo, M.W. Davidson, D.W. Piston, Fluorescent protein tracking and detection: fluorescent protein structure and color variants, Cold Spring Harb Protoc. 2009 (2009) pdb.top63.

[65] J.W.D. Comeau, S. Costantino, P.W. Wiseman, A guide to accurate fluorescence microscopy colocalization measurements, Biophys J. 91 (2006) 4611–4622.

[66] E.M.M. Manders, F.J. Verbeek, J.A. Aten, Measurement of co-localization of objects in dual-color confocal images, Journal of Microscopy. 169 (1993) 375–382.

[67] S.V. Costes, D. Daelemans, E.H. Cho, Z. Dobbin, G. Pavlakis, S. Lockett, Automatic and quantitative measurement of protein-protein colocalization in live cells, Biophys J. 86 (2004) 3993–4003.
[68] A. Revyakin, Z. Zhang, R.A. Coleman, Y. Li, C. Inouye, J.K. Lucas, et al., Transcription initiation by human RNA polymerase II visualized at single-molecule resolution, Genes Dev. 26 (2012) 1691–1702.

Acknowledgements

We thank Abdullah Al-Mahmood for preliminary FRAP development, and Ian Dobbie for technical microscopy support. We thank Ann McEvoy and Will Draper for advice on PALM. This work was funded by an EPSRC grant EP/G061009/1, the Biological Physical Sciences Institute (BPSI) at York University and Royal Society URF (M.C.L.), RCUK scholarships (O.H. and A.R.), Wellcome Trust VIP Award (T.L. and C.W.M.), Marie Curie Intra-European Fellowship FP7-PEOPLE-2009-IEF 254575 (L.-N.L.), NIH grant GM RO1 32543 (C.B.), Deutsche Forschungs Gemeinschaft FOR 929 (T.F.), and BBSRC grant BB/J016985/1 (C.W.M.).

The authors declare no competing interests

Supplementary Figures

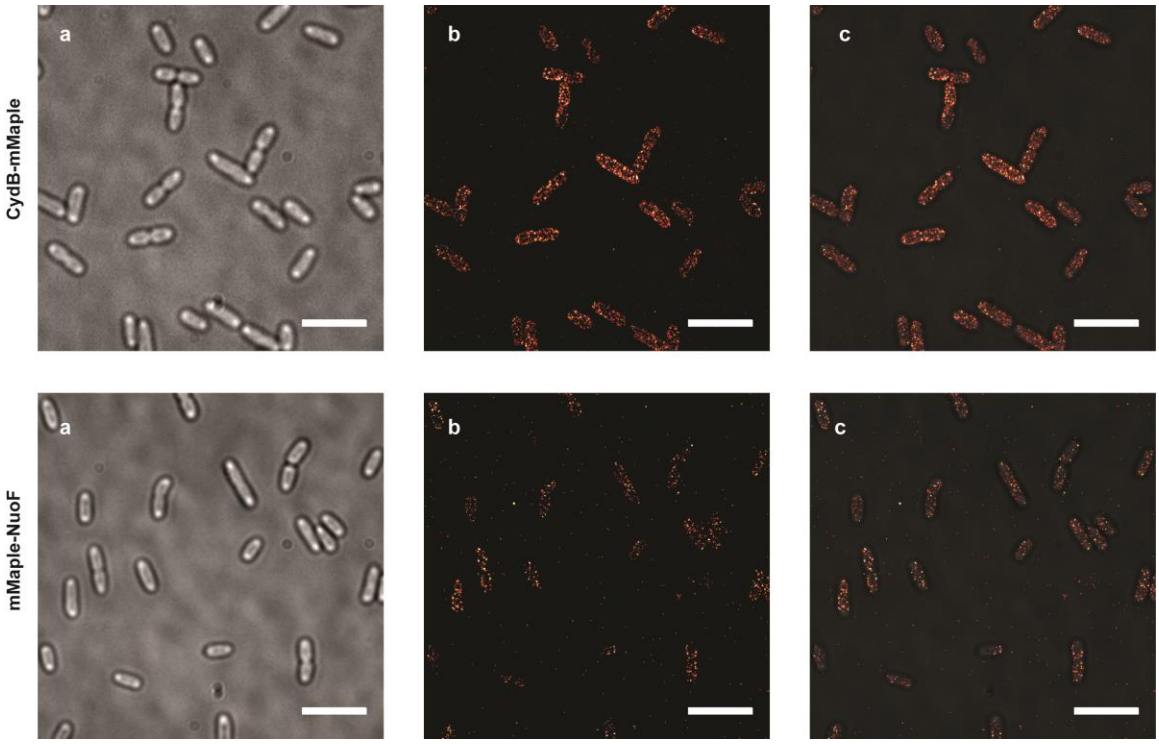

Supplementary Figure 1. Super-resolution imaging of OXPHOS complexes in Escherichia coli (fields of view showing multiple cells). Upper panels - CydB-mMaple; lower panels- mMaple-NuoF; **(a)** Brightfield; **(b)** Rendered PALM images of mMaple localizations; **(b)** overlay. White scale bars indicate 5µm.

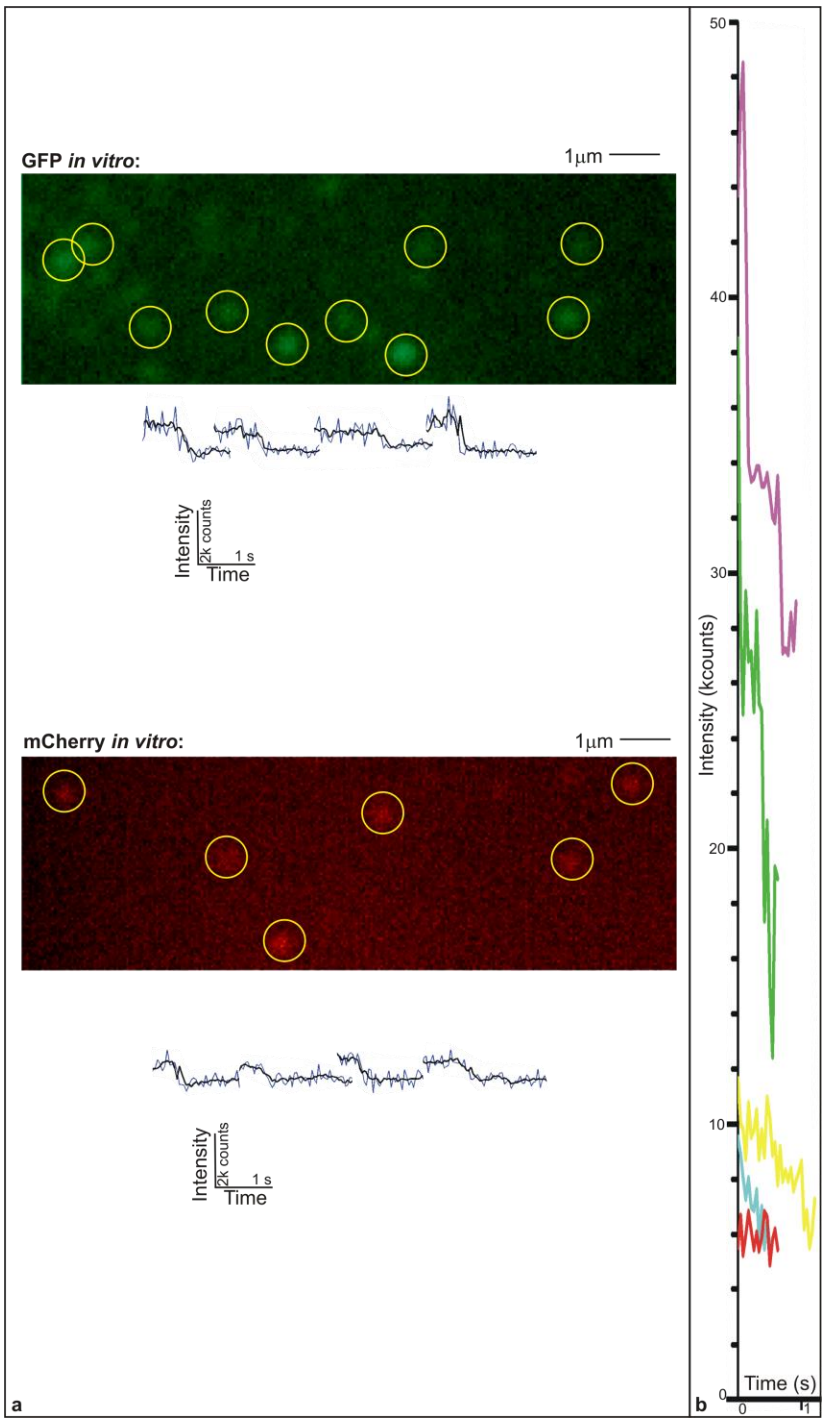

Supplementary Figure 2. (a) Brightness of purified fluorescent protein *in vitro*; Typical near-TIRF images of surface-immobilized GFP (upper panel) and mCherry (lower panel), with representative single-molecule photobleach traces showing raw spot intensity (blue) and Chung-Kennedy filtered (black). **(b)** Example intensity *vs* time photobleach traces *in vivo* for each OXPHOS protein studied of AtpB-GFP (magenta), CytdB-mCherry (green), SdhC-mCherry (yellow), NuoF-GFP (cyan), CyoA-mCherry (red), each example from a different cell.

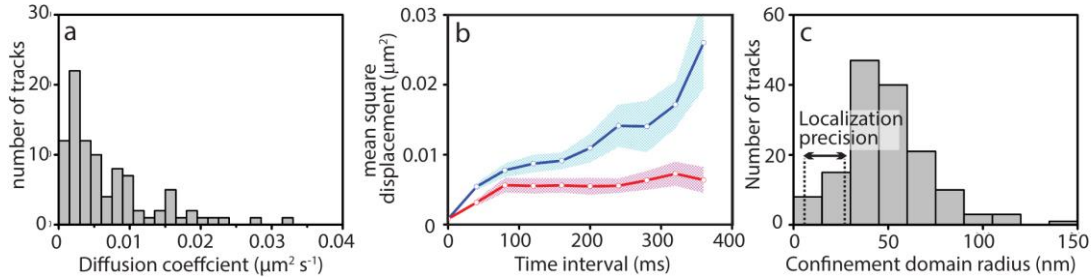

Supplementary Figure 3. Spot mobility analysis using Bayesian inference. **(a)** Distribution of Brownian diffusion coefficients across all cell strains. **(b)** Example of mean square displacements, here for pooled NuoF-GFP data, indicating mean Brownian (blue) and confined (red) trace, SEM error-bounds, *n*=33-60 tracks. **(c)** Distribution of effective confinement radius across all cell strains, range of tracking localization precision corresponding to measured spot intensities indicated (arrows). Diffusion coefficients and confinement radii are calculated on an individual track basis using BARD analysis.

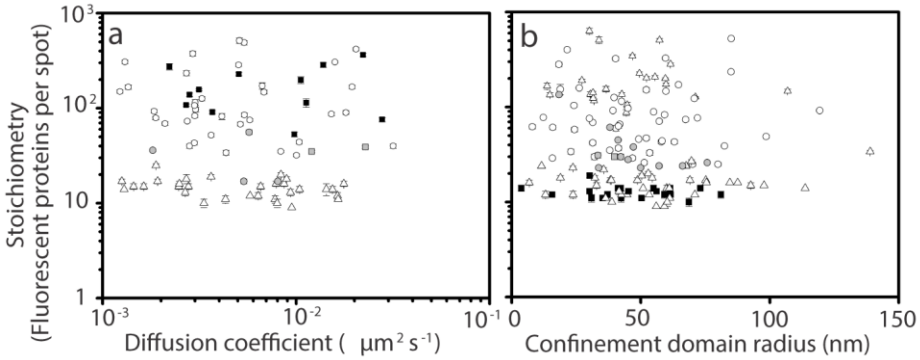

Supplementary Figure 4. Variation of **(a)** diffusion coefficient and **(b)** confinement radius versus fluorescent protein stoichiometry per spot: AtpB-GFP (white circles), CydB-mCherry (black squares), CyoA-mCherry (grey squares), NuoF-GFP (white triangles) and SdhC-mCherry (grey circles), error bars indicate s.d.

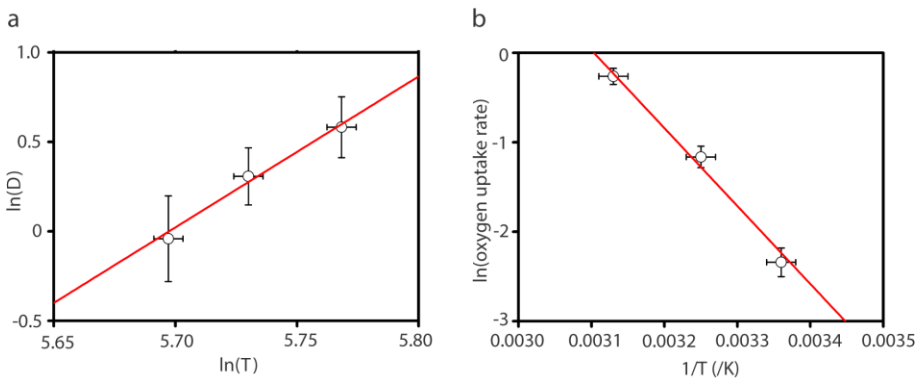

Supplementary Figure 5. Variation of **(a)** ln of diffusion coefficient D with ln of absolute temperature *T*, and **(b)** ln of oxygen uptake rate of cells with reciprocal of *T*, straight-line fits indicated (red), errorbars indicate s.d.

Supplementary Tables

Cell strains relevant to non-PALM fluorescence imaging:			
Strain name	**Cell doubling time (min), in LB, 37°C, ±SD**	**Cell doubling time (min), in M63-glucose, 37°C, ±SD**	**Cell doubling time (min), in M63-glucose, 23°C, ±SD**
BW25113 (wild type)	23±5	65±2	260±18
AtpB-GFP	21±6	58±1	-
NuoF-GFP	26±2	64±6	-
CydB-mCherry	34±9	61±5	-
CyoA-mCherry	36±5	64±2	-
SdhC-mCherry	33±12	82±25	-
NuoF-GFP:SdhC-mCherry	33±6	68±3	-
AtpB-GFP:CydB-mCherry	22±2	66±1	245±8
NuoF-GFP:CydB-mCherry	35±3	80±5	-
Cell strains relevant to PALM imaging:			
MG1655 (wild type)	34±2	-	-
CydB-mMaple	50±1	-	-
MG1655 ΔCytdB	100±12	-	-

Supplementary Table S1. Growth characterization of strains used in current study. For non-PALM fluorescence imaging, the doubling times should all be referenced against the parental wild type strain BW25113; for PALM imaging, the doubling times should be referenced against the parental wild type strain of MG1655.

Primer	Sequence (5'-3')
P18	GGTCTGTTGCCGTGGTGGTCACAGTGGATCCTGAATGTGCCGTCA
P19	GTTTTCCATGACAGTCTCCAGTTTGTTTCAGTTAAAACGTAG TAG
P20	TGGCACTTGGCGTATTTATCC
P21	TACTACGCGACAGCGAACATC
cydB-cs-F	CACCAAAGAAGATATTGAACGTAACACCCACTCTGTACGGCCTAT GCGGCCGCTAATATCAGAAGAACTCGTCAAGAAG
cydb-cs-R	GCGTTCCCAGAATCCATGCGAAATACCACATTTTTAGCTCCTTACG GATATTATCGTGAGGGTGC
cydB-maple-F	CACCAAAGAAGATATTGAACGTAACACCCACTCTCTGTACGGCCT ATGCGGCCGCATGGTGAGCAAGGGCGAGG
cydB-maple-R	GCGTTCCCAGAATCCATGCGAAATACCACATTTTTAGCTCCTTACT TACTTGTACAGCTCGTCCATG
nuoF- cs-F	GGACACTCACGCGCATCTGACCCCGGAAGCGATCCCTGAACTGCT GGAGCGGTATAATCAGAAGAACTCGTCAAGAAG
nuoF- cs-R	AGGTCAGCGGATGCGTTTCGGGAGTACGGATAATGTTTTTGGCCC TCAGGGCCGGATCCGTGGATATTATCGTGAGGGTGC
nuoF-maple-F	GGACACTCACGCGCATCTGACCCCGGAAGCGATCCCTGAACTGCT GGAGCGGTATAAATGGTGAGCAAGGGCGAGG
nuoF-maple-R	AGGTCAGCGGATGCGTTTCGGGAGTACGGATAATGTTTTTGGCCC TCAGGGCCGGATCCGTAGCGAGCTCCTGCAGCTTG

Supplementary Table S2: Oligonucleotide primer sequences

OXPHOS protein (Source cell strains)	Proportion of trajectories from all data inferred to be in each diffusion model (%)				Total number of tracks identified of duration ≥ 200ms
	Anomalous	Brownian	Confined	Directed	
NuoF (NuoF-GFP:SdhC-mCherry)	22.2	30.6	47.2	0	36
NuoF (NuoF-GFP:CydB-mCherry)	30.8	23.5	45.7	0	94
SdhC (NuoF-GFP:SdhC-mCherry)	5.6	27.8	66.7	0	18
AtpB (AtpB-GFP:CydB-mCherry)	29.1	29.1	41.8	0	134
CydB (NuoF-GFP:CydB-mCherry)	35.3	20.6	44.1	0	34
CydB (AtpB-GFP:CydB-mCherry)	46.1	15.4	38.5	0	26

Supplementary Table S3. OXPHOS protein mobility analysis, indicating proportion of trajectories from all data whose mobility were consistent with either anomalous, Brownian, confined or directed diffusion models using BARD analysis.

Labelled OXPHOS protein	Unconfined tracks (anomalous + Brownian + directed)	Confined tracks	Total
NuoF	70	60	130
CydB	78	56	134
AtpB	35	25	60
SdhC	6	12	18

Supplementary Table S4. Numbers of tracks of each protein predicted to have unconfined or confined diffusion according to BARD analysis. $\chi^2 = 4.306$, d.f.=3, $P = 0.23$ (non-significant).

Supplementary Movies

Movie S1 legend. Near-TIRF simultaneous dual-color movie of strain NuoF-GFP:SdhC-mCherry, indicating separate color channels of red (upper) and green (lower) of the same cell. Continuous frame sampling at 25 Hz shown in real-time with fixed grayscale pixel display scaling throughout.

Movie S2 legend. Near-TIRF simultaneous dual-color movie of strain AtpB-GFP:CydB-mCherry, indicating separate color channels of red (upper) and green (lower) of the same cell. Continuous frame sampling at 25 Hz shown in real-time with fixed grayscale pixel display scaling throughout.